JℲM PAPERS

On wall pressure fluctuations in conical shock wave/turbulent boundary layer interaction

Feng-Yuan Zuo[1],†, Antonio Memmolo[2] and Sergio Pirozzoli[3],†

[1]State Key Laboratory for Strength and Vibration of Mechanical Structures, School of Aerospace Engineering, Xi'an Jiaotong University, 710049 Xi'an, PR China

[2]HPC department, CINECA-Interuniversity consortium, via Magnanelli 2, I-40033 Casalecchio di Reno, Bologna, Italy

[3]Dipartimento di Meccanica e Aerospaziale, Sapienza Università di Roma, Via Eudossiana 18, 00184 Roma, Italy

The structure and the frequency spectra of wall pressure fluctuations beneath a planar turbulent boundary layer interacting with a conical shock wave at Mach number $M_\infty = 2.05$ and Reynolds number $Re_\theta \approx 630$ (based on the upstream boundary layer momentum thickness) are examined to elucidate the effects of pressure gradient and flow separation on the characteristics of the wall pressure fluctuations, by exploiting a direct numerical simulation database. Upstream of the interaction, in the zero pressure gradient region, wall pressure statistics compare well with canonical compressible boundary layers in terms of fluctuation intensities and frequency spectra. Across the main interaction zone (APG1), the root-mean-square of wall pressure fluctuations becomes very large (corresponding to approximately 173.3 dB), with maximum increase approximately 12.7 dB from the incoming level. In the second adverse pressure gradient zone (APG2), the root-mean-square of wall pressure fluctuations attains a second peak (corresponding to 164.7 dB), with an increase of 8.4 dB from the upstream level. Both the APG1 and APG2 regions feature a substantial fraction of flow reversal events, which are, however, scattered and interspersed with regions of attached flow. The wall pressure power spectral density exhibits a broadband and energetic low-frequency component associated with the global unsteadiness of the separation bubble/conical shock system. Analysis of the two-point correlations and wavenumber/frequency spectra of wall pressure fluctuations further suggests that the typical eddies become more elongated along the spanwise direction, as the flow in the separated region tends to escape the centreline, and the convection velocity is significantly reduced.

Key words: high-speed flow, compressible boundary layers, shock waves

† Email addresses for correspondence: fengyuan@xjtu.edu.cn, sergio.pirozzoli@uniroma1.it

F.-Y. Zuo, A. Memmolo and S. Pirozzoli

1. Introduction

Shock wave/boundary layer interaction (SBLI) has been investigated widely in the past few decades; see e.g. the review papers of Dolling (2001), Smits & Dussauge (2006), Clemens & Narayanaswamy (2014) and Gaitonde & Adler (2023). Typically, SBLIs have a detrimental influence on the flow behaviour, causing unwanted effects such as strong pressure fluctuations, structural fatigue fracture, and severe structural vibrations associated with unsteady pressure loads, especially in the presence of separation bubbles (Dupont, Haddad & Debieve 2006; Piponniau *et al.* 2009; Dupont, Piponniau & Dussauge 2019). Cases under consideration cover a large range of geometric configurations, including impinging planar shocks (Dupont *et al.* 2006; Robinet 2007; Humble *et al.* 2009; Piponniau *et al.* 2009; Pirozzoli & Bernardini 2011*a*; Touber & Sandham 2011; Sandham *et al.* 2014; Pasquariello, Hickel & Adams 2017; Lusher & Sandham 2020), over-expanded nozzles (Martelli *et al.* 2017), compression ramps (Adams 2000; Ganapathisubramani, Clemens & Dolling 2007; Wu & Martin 2008; Priebe & Martin 2012; Exposito, Gai & Neely 2021; Helm, Martin & Williams 2021) and transonic normal shock waves (Pirozzoli, Bernardini & Grasso 2010; Burton & Babinsky 2012; Sartor *et al.* 2015; Karnick & Venkatraman 2017). Despite the efforts of the research community, the physical mechanisms involved in SBLIs are not yet completely understood, especially concerning the low-frequency unsteadiness associated with the separation shock, whose frequencies are approximately two orders of magnitude lower than those of the upstream boundary layer, and whose underlying cause is still debated (Priebe *et al.* 2016; Adler & Gaitonde 2020; Ceci *et al.* 2023; Gaitonde & Adler 2023).

The prediction of pressure fluctuations plays an important role in the vibro-acoustic design in the high-speed regime, such as for launch vehicles. The induced vibrations in the inner vehicle can extremely exceed design specifications and cause payload damage (Camussi *et al.* 2007). Calculations of structural dynamics require the knowledge of the space–time correlations of the wall pressure field as a forcing input (Cebral & Lohner 1997). A big effort has been devoted by researchers to low-speed flow, whereas much more scattered data are present for the high-speed regime. An experimental representation of the unsteady wall pressure signature for the high-speed regime, especially for flows in adverse pressure gradient (APG), is challenging, owing to limitations both on the maximum frequency resolution of pressure transducers and on the spatial resolution, due to the relatively big size of the sensors with respect to the small spatial scale of turbulence, which results in a sensor averaging effect. An accurate characterization requires the use of high-fidelity calculations (Bernardini, Pirozzoli & Grasso 2011; Morgan *et al.* 2013), including direct numerical simulations (DNS) and large-eddy simulations (LES).

The behaviour of wall pressure fluctuations has attracted significant attention in the past several decades. Schloemer (1967) carried out an experimental study in a low-turbulence subsonic wind tunnel, focusing on the influence of both mild APG and mild favourable pressure gradient (FPG) on the wall pressure fluctuations. He concluded that mild APG increases wall pressure spectral densities at low frequencies in outer scaling, whereas the high-frequency range is much less affected, while mild FPG causes a sharp decrease in the high-frequency portion. Mabey (1972) analysed experimental data of the root-mean-square (r.m.s.) of wall pressure fluctuations p_{rms} in separated flow at subsonic speeds. That author found that the pressure fluctuations caused by bubbles increase gradually from the separation line, reaching a maximum value near the reattachment line, and then decrease gradually downstream. Kiya & Sasaki (1983) conducted an experimental study on the flow in the separation bubble formed at the leading edge of a blunt flat plate. Based on

the cross-correlations between surface pressure and velocity fluctuations, they reported that there exists a large-scale unsteadiness in the bubble, and also a large p_{rms} near reattachment, supporting the experimental data of Mabey (1972). Measurements of surface pressure fluctuation spectra for a separating turbulent boundary layer were reported by Simpson, Ghodbane & McGrath (1987). They found that the wall pressure fluctuations increase monotonically through both attached and detached regions under APG conditions, and showed that the maximum in the wall-normal direction of the turbulent shear stress $\tau_m = \max_y(-\bar{\rho}\,\widetilde{u''v''})$ yields good universality of the spectra. More recently, Mohammed & Weiss (2016) investigated experimentally the unsteady behaviour of pressure-induced separation of a turbulent bubble at low speed, and demonstrated that the maximum wall pressure fluctuations near reattachment are associated with vertical velocity fluctuations in the shear layer.

A large amount of data comes from experiments, but also numerous high-fidelity numerical simulations have been conducted. Na & Moin (1998) carried out DNS of a turbulent boundary layer developing over a flat plate under APG conditions. The frequency spectra in the separation bubble, using outer scaling for times and local maximum of the Reynolds shear stress for pressure, were found to exhibit a slope close to an ω^{-4} scaling law at high frequencies. The analysis of two-point correlations of wall pressure fluctuations inside the separation bubble in the spanwise direction implies the presence of large two-dimensional roller-type structures. Wu & Moin (2009) conducted DNS of a zero pressure gradient (ZPG) incompressible boundary layer over a smooth flat plate, finding that the frequency spectra of wall-normal velocity fluctuations in the turbulent region, where scaled with δ/u_τ^3, exhibit an $\omega^{-5/3}$ scaling at intermediate frequencies, and an ω^{-7} power-law decay at the high-frequency range. Bernardini *et al.* (2011) performed DNS of transonic normal SBLI at $M_\infty = 1.3$, finding that the pressure spectra, using outer scaling for times and local maximum of the Reynolds shear stress for pressure, exhibit an $\omega^{-7/3}$ power law in the subsonic APG region at intermediate frequencies, and an ω^{-5} decay at high frequency. Based on the analysis of pressure sources in Lighthill's equation, they found that the contributions to low-frequency pressure fluctuations are associated with long-lived eddies developing far from the wall. Ji & Wang (2012) investigated the pressure fluctuations in subsonic flows over a backward- or forward-facing step with LES. They found that the pressure spectrum at the maximum p_{rms} location rolls off with a slope close to $-7/3$ at high-frequency range, in a good agreement with the observations of Bernardini *et al.* (2011). Abe (2017) continued research of Na & Moin (1998) based on DNS at different Reynolds number ($Re_\theta = 300, 600, 900$), finding that the scaling law of p_{rms} exhibits good agreement in the APG region with the data of Na & Moin (1998), at low frequencies. Recently, Adler & Gaitonde (2020, 2022) carried out an LES study to investigate the unsteadiness in three-dimensional (3-D) sharp-fin and swept-compression-ramp interactions. They found that flow separation in 3-D interactions is topologically different than two-dimensional (2-D) SBLIs. The prominent band of low-frequency unsteadiness ($Sr_L \approx 0.03$) is found to be significantly reduced in 3-D SBLIs. Zuo, Memmolo & Pirozzoli (2021) carried out a Reynolds-averaged Navier–Stokes (RANS) simulation study of conical shock/boundary layer interactions (CSBLIs), finding that reasonable estimates of the variance of pressure fluctuations can be obtained in a post-processing stage, by extending the analogy between turbulent shear stress and p_{rms}.

The available data do not bring a conclusive description of the wall pressure behaviour in supersonic boundary layers, and DNS are a valuable tool to get access to all flow statistics. On the other hand, in hypersonic flight, due to the recent development of integrated design techniques, wave-rider vehicles and wave-catcher (inward-turning) intakes are required to
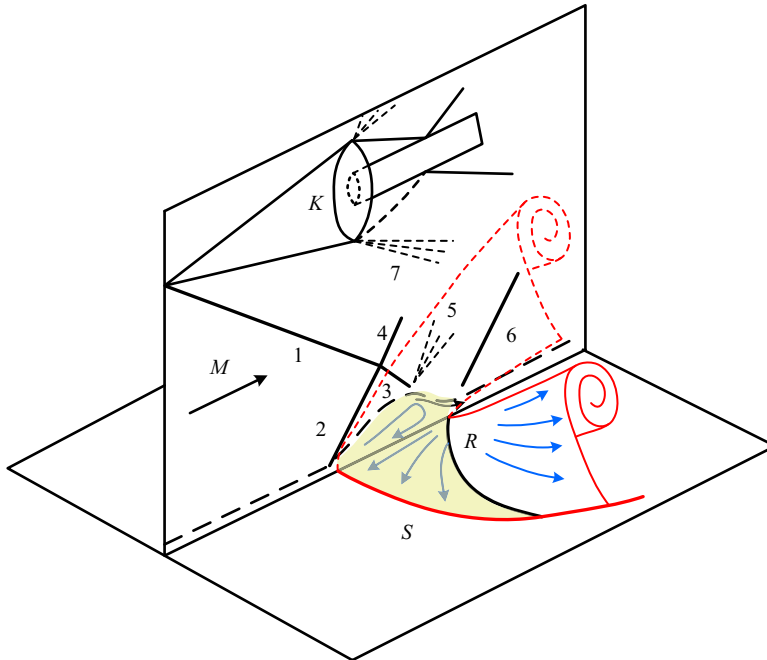
Figure 1. Flow-field structure of strong CSBLI under separation condition. Numbered solid lines are conical shock traces; numbered dashed lines are rarefaction waves. The shadow is the separation bubble, delimited in the wall plane by *S* (separation) and *R* (reattachment).

achieve better aerodynamic performance (Zuo & Mölder 2019). The price to pay is a more complicated internal flow field, with an unavoidable CSBLI within rockets or intakes in both external and internal flow. To our knowledge, the only DNS of CSBLI have been performed only recently by the present authors (Zuo *et al.* 2019).

The analysis of CSBLI is inherently more difficult than for planar SBLI, in that the flow field past a conical shock is not uniform, and the wall pressure rise is not uniform along the boundary layer transverse direction, hence the resulting limiting wall streamlines are not parallel. Moreover, non-uniformity of the imposed shear yields a variety of complex vortical structures that interact and merge while becoming entrained in the main flow. A greater challenge is also encountered in the numerical simulation of CSBLI, mainly because of slow convergence of the flow statistics in the absence of directions with spatial homogeneity. The leading features of CSBLI are sketched in figure 1, based on recent DNS results (Zuo *et al.* 2019). The shock generator *K* generates the incident conical shock 1, and 2 is the 3-D separation shock associated with separation of the boundary layer. The approaching flow that passes through shock 2 is deflected upwards, and after passing through shock 3 and rarefaction wave 5, the separated boundary layer is directed at some angle towards the plate surface. Shock 6 then arises to realign the outer flow to the wall-parallel direction. The boundary layer, which separates along line *S* (coalescence line), reattaches along line *R* (divergence line). As in the case of the later analysis, the rarefaction wave 7 emanating from the shock-generating device can also enter into play, thus further complicating the analysis of the flow in the interaction region. The overall phenomenon, with special reference to the separation region, is inherently 3-D in nature.

The objective of the present work is the analysis of the wall pressure statistics, where pressure fluctuations are induced by the statistically 3-D CSBLI. The analysis is carried

out on a DNS database obtained at a low Reynolds number, describing a conical shock wave interacting with a turbulent boundary layer developing on a flat plate. The conical shock is generated by a 3-D cone immersed in a supersonic stream, at free-stream Mach number $M_\infty = 2.05$ and with half-cone angle $\theta = 25°$. The length of the cone is finite, so that the main shock is followed by an expansion region due to the deflection of the flow passing from the side wall of the cone to its base, with subsequent recompression waves due to the wake closure. The wave system induced by the cone has a strong impact on the boundary layer dynamics, also reflected by the wall pressure field. The selected flow conditions correspond as closely as possible to the reference experiment of Hale (2015), from which data gathered by means of surface oil flow, pressure-sensitive paint and particle image velocimetry are available for comparison.

This paper is organized as follows. In § 2, the numerical method and the DNS database are described. The instantaneous and mean flow configurations are reported in § 3. Five representative stations in the different flow regimes are identified in § 3.3. The analysis of the wall pressure fluctuations is reported in § 4. The pressure fluctuation distributions are discussed in § 4.1. The power spectral density (PSD) of the wall pressure signal in CSBLI is analysed in § 4.2, and the two-point correlation and space–time correlations are reported in §§ 4.3 and 4.4. Concluding remarks are given in § 5.

2. Computational strategy

Navier–Stokes equations for a perfect Newtonian gas with constant Prandtl number and variable molecular viscosity given by Sutherland's law are considered. A conservative discretization of convective derivatives is carried by means of sixth-order central differences away from shocks, applying the same splitting as Pirozzoli (2010), which enforces nonlinear stability without recurring to numerical diffusion. In shocked regions, the scheme is combined with a seventh-order weighted essentially non-oscillatory (WENO) discretization, as controlled by a sensor based on the ratio of local dilatation to vorticity modulus (Pirozzoli 2011). The diffusive terms are also discretized with sixth-order central differences, after being expanded in Laplacian form to avoid odd–even decoupling. Time advancement is carried out by means of a third-order explicit Runge–Kutta integration algorithm. The complete description of the used computational strategy can be found in our previous study (Zuo *et al.* 2019).

2.1. *Computational domain*

The used computational domain is sketched in figure 2, with streamwise extent $L_x = 150\delta_{in}$ (where δ_{in} is the inflow boundary layer thickness), spanwise length $L_z = 60\delta_{in}$, domain height $L_y = 30\delta_{in}$, and discretized with a grid including $1536 \times 384 \times 1280$ nodes. Uniform spacing is used in the streamwise and spanwise directions, whereas nodes are clustered in the wall-normal (y) direction up to $y/\delta_{in} = 6.5$. Streamwise and spanwise spacings are $\Delta x^+ \approx 10$ and $\Delta z^+ \approx 5$, respectively, whereas the spacing in the wall-normal direction ranges between 0.7 at the wall and 12. Here and elsewhere, the $+$ superscript is used to denote normalization with respect to the friction velocity $u_\tau = \sqrt{\tau_w/\rho_w}$ (where τ_w and ρ_w are the wall shear stress and density), and the viscous length scale is $\delta_v = \nu_w/u_\tau$ (where ν_w is the wall kinematic viscosity). The domain and its discretization are the same as employed in our previous work (Zuo *et al.* 2019; Zuo, Yu & Pirozzoli 2022), where we show that it is sufficient to simulate the physics of the flow correctly.
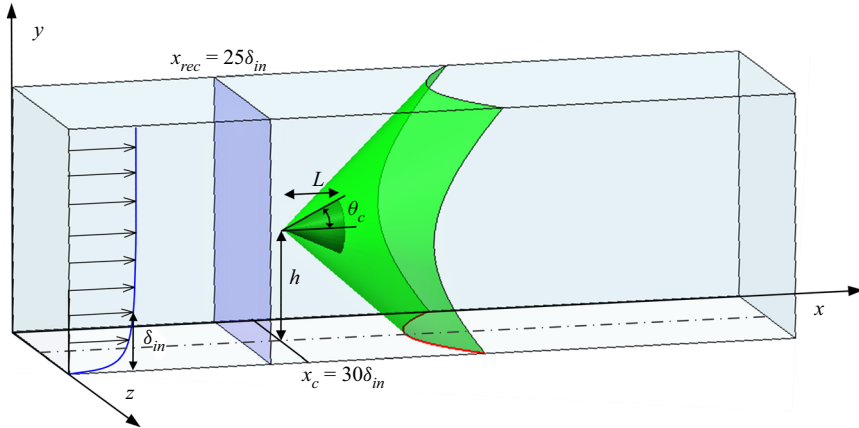
Figure 2. Sketch of computational domain for CSBLI analysis. Here, δ_{in} is the inflow boundary layer thickness, x_{rec} is the boundary layer recycling station, and x_c is the x coordinate of the cone leading edge. The green surface depicts the conical shock, whose wall trace is highlighted in red.

2.2. *Treatment of the shock generator*

We rely on the immersed boundary method (Fadlun *et al.* 2000) to accommodate the conical shock generator in the simulation. Solid and fluid nodes are located by means of a ray tracing algorithm (O'Rourke 1998). Interface nodes are fluid nodes whose stencil includes solid nodes, and on which flow parameters are imposed explicitly according to an equilibrium wall function (Tessicini *et al.* 2002). Implementation details are provided in Bernardini, Modesti & Pirozzoli (2016). The cone is resolved with approximately 72, 56 and 138 grid intervals in the streamwise, wall-normal and spanwise directions, respectively. As proven in Zuo *et al.* (2019), although the boundary layer on the cone is certainly not well resolved, this is not a major shortcoming, as the cone serves simply as a disturbing element to force a spatially varying pressure gradient onto the underlying boundary layer.

2.3. *Flow conditions*

The flow conditions are selected to be as close as possible to the reference experiment of Hale (2015). The shock generator is a cone with height $L/\delta_{in} = 6.835$ and half opening angle $\theta_c = 25°$. The apex of the cone is at $x_c = 30\delta_{in}$ from the inflow, and its axis is parallel to the wall at a distance $h/\delta_{in} = 13.67$ (see figure 2). The upstream flow has Mach number $M_\infty = 2.05$, and the Reynolds number based on the inflow boundary layer thickness is $Re_{\delta_{in}} = 5000$. The latter is approximately a factor of fifty less than the reference experiment, but as shown in Zuo *et al.* (2019), this is not the cause of major quantitative differences.

A realistic boundary layer is achieved through a rescaling–recycling procedure (Xu & Martin 2004), whereby a cross-stream slice of the flow field is extracted at every Runge–Kutta sub-step at the recycling station x_{rec}, and fed back to the inflow upon suitable rescaling. To minimize spurious time periodicity that may result from application of quasi-periodic boundary conditions in the streamwise direction, the recycling station is set at $x_{rec} = 25\delta_{in}$, also sufficiently upstream of the cone apex. Non-reflecting characteristic boundary conditions are applied to the outflow, at the top boundary, and in the spanwise direction for $x > x_{rec}$, whereas spanwise periodicity is assumed for $x \leq x_{rec}$.

Station	x/δ_{in}	Re_θ	Re_τ	$\bar{p}_w/p_\infty$	ρ_e/ρ_∞	u_e/u_∞	δ^*/δ	θ/δ
1	27.5	670	160	1.00	1.00	1.00	0.303	0.088
2	35.0	735	170	1.00	1.00	1.00	0.305	0.089
3	42.0	900	105	1.11	1.00	1.00	0.309	0.102
4	44.0	1050	125	1.34	1.46	0.88	0.458	0.101
5	50.0	920	235	1.35	1.16	0.96	0.289	0.115
6	60.0	680	175	0.75	0.83	1.03	0.293	0.073
7	72.0	810	150	0.77	0.91	1.01	0.358	0.069
8	75.0	1095	145	0.90	0.93	1.01	0.331	0.094
9	120.0	1400	270	1.00	0.99	0.99	0.330	0.100
10	140.0	1510	285	1.00	0.98	1.00	0.323	0.100

Table 1. Boundary layer properties at selected streamwise stations for pressure field analysis. Subscripts: e indicates properties at the edge of the boundary layer; w indicates wall properties; and ∞ indicates free-stream properties. Here, $Re_\theta = \rho_e u_e \theta/\mu_e$ is the Reynolds number based on the momentum thickness θ of the boundary layer, and $Re_\tau = \rho_w u_\tau \delta/\mu_w$ is the friction Reynolds number.

Unsteady characteristic boundary conditions are specified at the bottom no-slip wall (Poinsot & Lele 1992), with temperature set to its adiabatic value. Flow statistics have been collected from time $t_0 u_\infty/\delta_{in} \approx 1711$ to time $t_f u_\infty/\delta_{in} \approx 3461$, at intervals of $\Delta t\, u_\infty/\delta_{in} \approx 0.1$. The long sampling time is needed to achieve convergence of pointwise statistics in time in the absence of homogeneous directions, and it makes the present calculation quite time-consuming. The statistical analysis is carried out by splitting the instantaneous quantities into their mean and fluctuating components, using either the standard Reynolds decomposition $f = \bar{f} + f'$, or the density-weighted (Favre) decomposition $f = \tilde{f} + f''$, where $\tilde{f} = \overline{\rho f}/\bar{\rho}$.

2.4. *Assessment of flow properties*

A necessary check is that the incoming boundary layer is developed properly prior to interaction with the conical shock. For that purpose, we consider a reference station at $x_{ref} = 27.5\delta_{in}$, located upstream of the cone leading edge. The global boundary layer properties at this station are listed in table 1, where δ is the 99 % thickness, δ^* is the displacement thickness,

$$\delta^* = \int_0^{\delta_e} \left(1 - \frac{\bar{\rho}}{\rho_e} \frac{\bar{u}}{u_e}\right) \mathrm{d}y, \tag{2.1}$$

and θ is the momentum thickness,

$$\theta = \int_0^{\delta_e} \frac{\bar{\rho}}{\rho_e} v \frac{\bar{u}}{u_e} \left(1 - \frac{\bar{u}}{u_e}\right) \mathrm{d}y, \tag{2.2}$$

with the upper integration limit δ_e denoting the edge of the rotational part of the boundary layer, defined as the point where the mean spanwise vorticity becomes less than $0.005 u_\infty/\delta_{in}$ (Pirozzoli *et al.* 2010). The subscript e is used to denote the corresponding external flow properties.
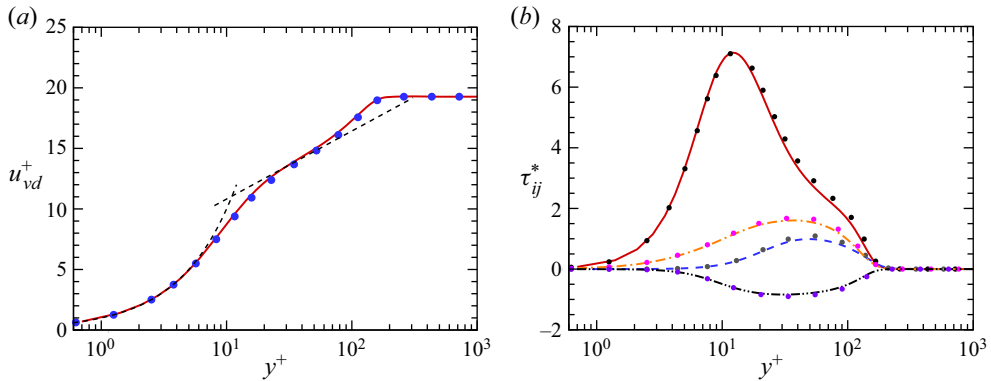
Figure 3. (*a*) The van Driest transformed mean streamwise velocity, and (*b*) density-scaled turbulent stresses, at the reference station ($x_{ref} = 27.5\delta_{in}$). Lines refer to the present DNS data, and symbols to reference data (Pirozzoli & Bernardini 2011*b*). In (*a*), the dashed line denotes a compound of $u^+ = y^+$ and $u^+ = 5.2 + 1/0.41 \log y^+$. In (*b*), we show τ_{11}^* (solid), τ_{22}^* (dashed), τ_{33}^* (dash-dotted) and τ_{12}^* (dash-dot-dotted).

The van Driest effective velocity,

$$u_{vd} = \int_0^{\bar{u}} \left(\frac{\bar{\rho}}{\bar{\rho}_w} \right)^{1/2} d\bar{u}, \tag{2.3}$$

is used in figure 3(*a*) to compare with boundary layer data at similar flow conditions (Pirozzoli & Bernardini 2011*b*). Comparison with the reference data is quite good, and in particular, the velocity profiles show linear behaviour up to $y^+ \approx 5$, as expected for adiabatic boundary layers (Smits & Dussauge 2006), and a narrow range with near logarithmic variation. Comparison of the density-scaled velocity correlations

$$\tau_{ij}^* = \frac{\bar{\rho} \, \widetilde{u_i'' u_j''}}{\tau_w} \tag{2.4}$$

is also shown in figure 3(*b*). The agreement with the reference data is again quite good, which leads us to conclude that the upstream boundary layer corresponds well to a healthy state of equilibrium wall turbulence. Full validation of the DNS data is reported in Zuo *et al.* (2019).

3. Flow structure

3.1. *Symmetry plane*

The detailed flow features have been reported in our previous work (Zuo *et al.* 2019). In this subsection, we limit ourselves to the description of the main characteristics, showing some slices for both mean and instantaneous configurations. Figure 4 shows the magnitude of the density gradient (numerical schlieren) on the symmetry plane, to highlight the overall wave system. Upstream of the interaction, the turbulent boundary layer develops and propagates downstream, creating numerous vortices lifting off the wall surface. At the impingement point, two reflected shock waves appear, indicating flow reversal. The first reflected shock is induced by the boundary layer separation, while the second shock is caused by the subsequent reattachment. Between these two shocks, an expansion fan is observed, as in the case of planar SBLI (Piponniau *et al.* 2009; Pirozzoli & Bernardini 2011*a*).
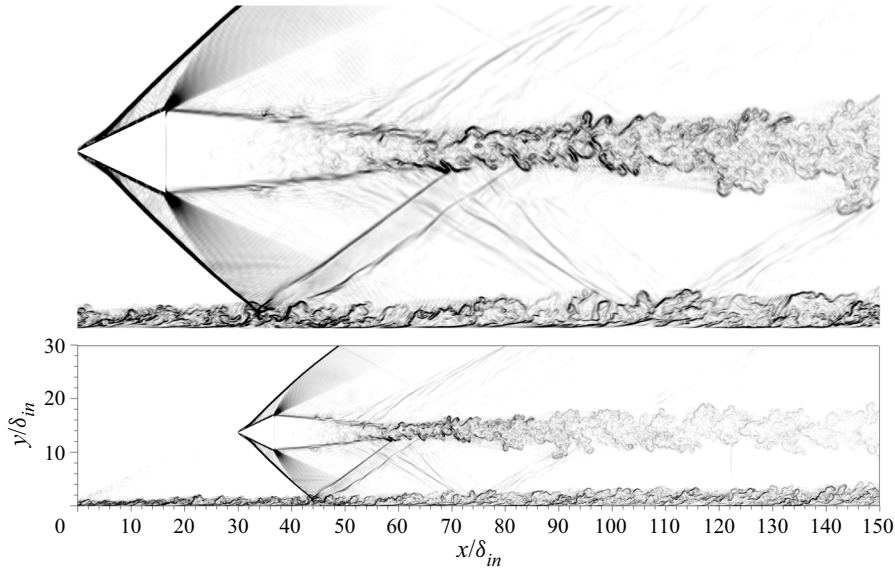
967 A3-8

Figure 4. Overall structure of the CSBLI. The cone geometry is blanked, and shock waves are shown by means of numerical schlieren, defined through the magnitude of the density gradient ($-1.0 \times |\nabla \rho|$). Contours are in the range $-1.0 < -1.0 \times |\nabla \rho| < -0.04$, from black to white.

Focusing on the flow in the cone proximity, the expansion fan originating at its trailing edge is also seen clearly in figure 4, interacting with both the incident and reflected shocks. The cone wake is also seen interacting with the main stream, giving rise to a turbulent mixing layer. The flows shear each other in this mixing region, seeding streamwise vortices downstream. These vortices propagate up to the end of the computational domain. The reflected conical shock arising from the main interaction at approximately $x \approx 45\delta_{in}$ impinges on the mixing layer and seems to disappear. Due to the expansion fan coming from the cone, the boundary layer relaxes under an FPG condition, becoming thinner, as shown clearly in figure 5, for the horizontal coordinate comprised between approximately $50\delta_{in}$ and $70\delta_{in}$. After this location, the compression fan due to wake closure leads to a second APG region, and the boundary layer thickens again. The qualitative effects on the boundary layer thickness are revealed clearly in figure 5. The overall qualitative description of the flow is completed in supplementary movies 1 and 2, including the instantaneous streamwise velocity flow field and numerical schlieren defined through the magnitude of the density gradient (see supplementary movies available at https://doi.org/10.1017/jfm. 2023.480).

3.2. *Wall surface*

The contours of the mean wall pressure are shown in figure 6(*a*). As the flow proceeds downstream, it encounters a first APG region (APG1), caused by the incident conical shock, which may be visualized by the black solid line in the same figure. This line is the nominal shock trace for inviscid flow, which for a conical shock intersecting a plane wall has the equation

$$(x - x_c)^2 - \left(\frac{z}{\tan \alpha}\right)^2 = \left(\frac{h}{\tan \alpha}\right)^2, \tag{3.1}$$

where $x_c = 30\,\delta_{in}$ is the cone leading edge, $\alpha = 41.85°$ is the conical shock angle, and $h = 13.67\,\delta_{in}$ is the distance of the cone axis from the wall. As can be seen, pressure after the
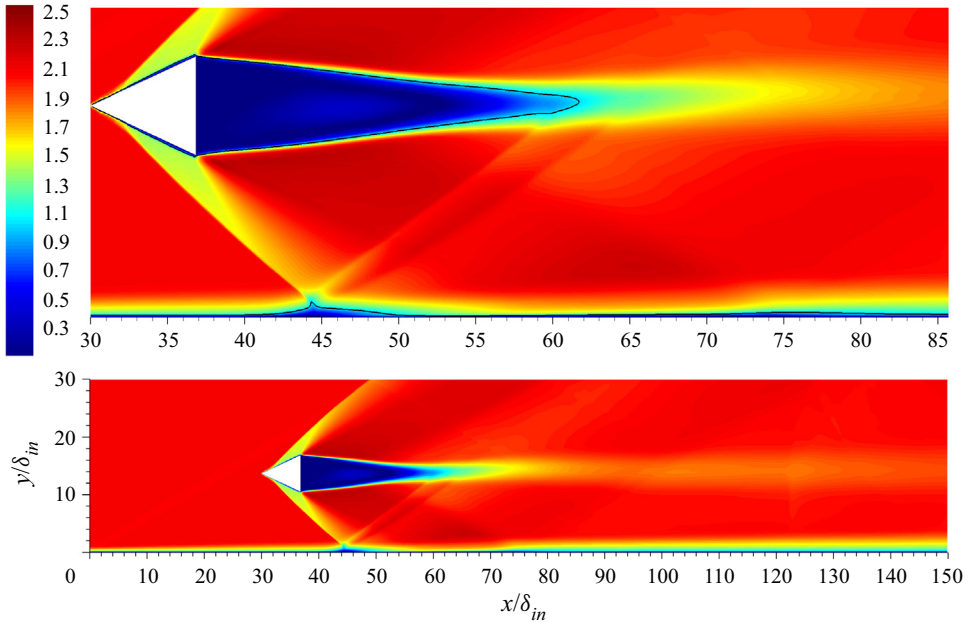
Figure 5. Mean Mach number contours in the streamwise, wall-normal plane, with $0.1 < M < 2.5$, and contour levels from blue to red. The black solid line indicates the sonic line.

shock trace is not uniform, but rather has a maximum on the symmetry line and decreases as the distance from the symmetry line increases, leading to a flow deflection away from the symmetry line. Moving along the streamwise direction, the flow then experiences an expansion, followed by a second horseshoe pattern of a high pressure region (APG2), corresponding to the compression waves generated by the wake closure behind the cone.

Contours of the r.m.s. of wall pressure fluctuations are shown in figure 6(*b*) in dB scale, assuming $p_\infty = 1$ atm. Strong spatial connection of this distribution is found with that of the vortical structures, shown in previous studies (Zuo *et al.* 2019). In particular, the largest values of p_{rms} are found at the interacting shock foot, especially around the symmetry axis where the shock is stronger. Consistent decrease of the fluctuating pressure loads is observed past the incident shock in the FPG region, which is depleted with eddies, as shown in our previous paper (Zuo *et al.* 2019). The vortices tend to disappear in the FPG region, and to reform past the recompression shock; however, setting a lower threshold for the vortex identification criterion would still show weaker eddies in the expansion zone. A secondary peak is observed further downstream, corresponding to reformation of the vortical structures. Numerical artefacts should be noted at the side boundaries, which are due to the imperfect nature of the numerical radiating boundary conditions, especially in the presence of waves not propagating orthogonally to the computational boundary. These effects are, however, confined to a narrow layer adjacent to the boundaries.

3.3. *Identification of flow regimes*

The distribution of the r.m.s. of pressure fluctuations (p_{rms}) in the symmetry plane is reported, again in dB scale, in figure 7. The figure shows that the pressure fluctuations attain maximum values in the mixing layer near the primary interaction zone. The pressure fluctuations increases again at approximately $x/\delta_{in} = 75$, in correspondence with the APG2 region. Large values of pressure fluctuations are also observed in the wake of
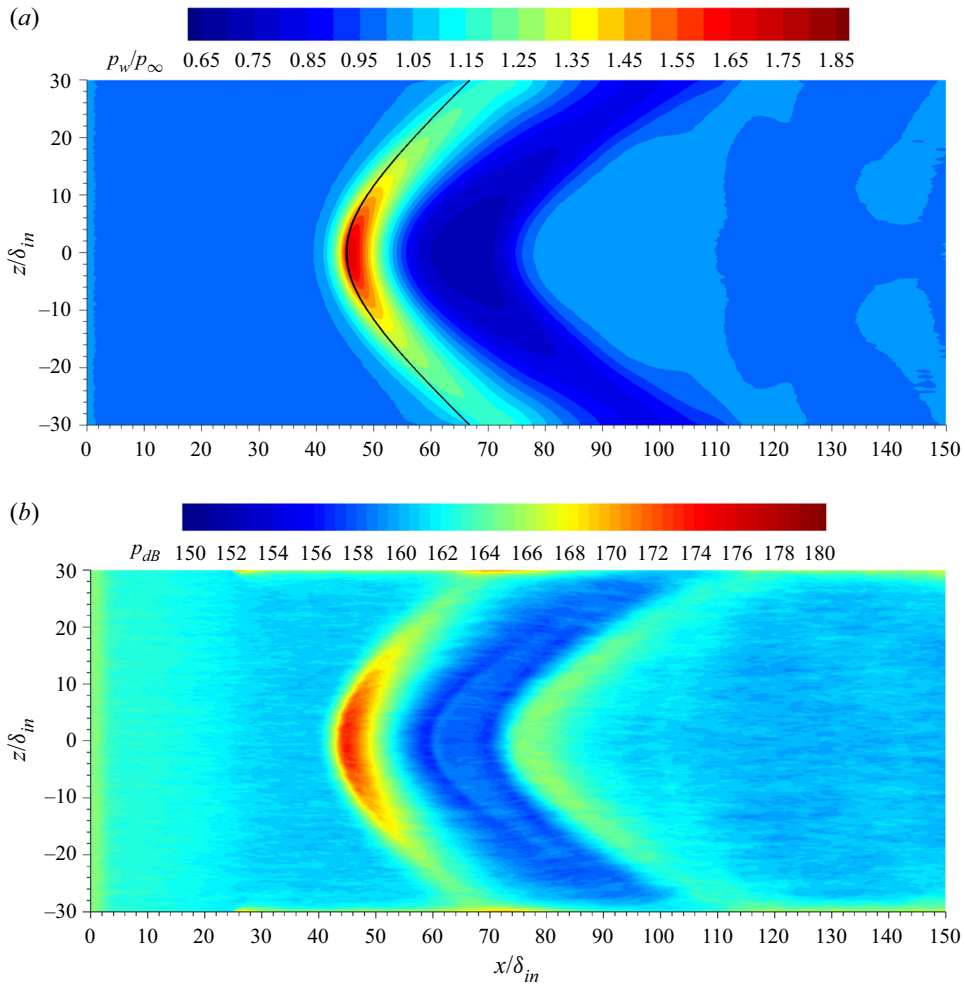
967 A3-10

(*a*)

(*b*)

Figure 6. (*a*) Contours of time-averaged wall pressure p/p_∞, with 27 contour levels, ranging from 0.6 to 1.9, from blue to red. The black line indicates the inviscid shock trace. (*b*) Contours of r.m.s. of wall pressure fluctuations, in dB scale, $p_{dB} = 20 \log_{10}(p'/(2 \times 10^{-5} \text{ Pa}))$, assuming $p_\infty = 1$ atm. Contour levels are shown from 150 to 180, from blue to red.

the conical device that we use to generate the shock, as a result of vortex shedding. When analysing the boundary layer properties, with particular reference to the computation of the local maximum in the wall-normal direction of the Reynolds shear stress, the cone wake must not be considered, else it would lead to a miscalculation of the local maximum. A simple fix to this problem is to consider the maximum not over all y, but only up to the boundary layer edge.

For clarity in the illustration of the results, the boundary layer properties at selected streamwise stations are summarized in table 1. Station 1 is the reference station where the profiles of figure 3 were taken, and together with station 2, located just upstream of the start of APG1, they are representative of the first ZPG zone (ZPG1) of the flow. Stations 3 and 4 are taken in the virtual origins of separation and reattachment shocks, respectively, inside the APG1 zone. Stations 5 and 6 are inside the FPG zone of the flow, whereas stations 7 and 8 are inside the APG2 zone. Finally, stations 9 and 10 correspond to the second ZPG zone (ZPG2), in the supersonic recovery region.
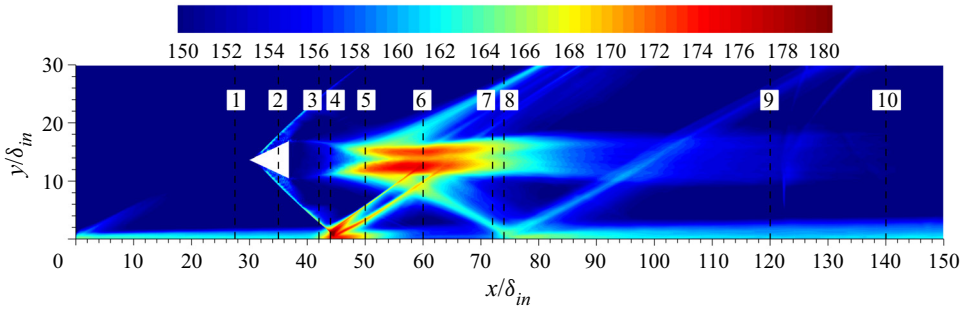
Figure 7. Contours of r.m.s. of pressure fluctuations (p_{rms}) in the symmetry plane, in dB scale, $p_{dB} = 20 \log_{10}(p_{rms}/(2 \times 10^{-5}\ \text{Pa}))$, assuming $p_\infty = 1$ atm. Contour levels are shown from 150 to 180, from blue to red. The blank region corresponds to the shock generating device. Boxed numbers identify the streamwise stations 1–10, referenced in table 1.

The distributions of the average pressure coefficient $C_p = (p - p_\infty)/q_\infty$ and average friction coefficient $C_f = \tau_w/q_\infty$ ($q_\infty = 1/2\rho_\infty u_\infty^2$) on the symmetry line at the wall surface are reported in figure 8. At the wall surface, the wall shear stress τ_w is obtained as

$$\tau_w = \mu_w \left[\left(\frac{\partial \bar{u}}{\partial y} \right)^2 + \left(\frac{\partial \bar{w}}{\partial y} \right)^2 \right]^{1/2}. \tag{3.2}$$

As found in experiments by Hale (2015) and Gai & Teh (2000), the wall pressure shown in figure 8(*a*) exhibits a distinctive N-wave signature, with a sharp peak right past the precursor shock generated at the cone apex, followed by an extended zone with FPG, and terminated by the trailing shock associated with recompression in the wake of the cone. From figure 8(*b*), it can be seen clearly that the boundary layer separates in the first APG zone. Based on the negative values of C_f, we can mark the separation region in the range $x/\delta_{in} = 43$–45, and C_f attains its minimum value at $x/\delta_{in} \approx 44$. The skin friction then undergoes a sudden rise through the FPG region, after which it exhibits a drop, attaining a local minimum value in the second APG region, followed by a slow recovery process. This local minimum is, however, still higher than zero, reflecting that no mean separation occurs in the second APG zone. Upstream of the interaction zone and in the downstream ZPG2 region, the friction coefficient well follows the power-law behaviour predicted by simple theory (Smits & Dussauge 2006), namely

$$C_f = k\, Re_x^{-1/7}, \tag{3.3}$$

with $k = 0.0192$, with the obvious exception of the inflow region, where the boundary layer is not yet properly developed.

Non-equilibrium states of boundary layers upon imposed pressure gradient are traditionally analysed in terms of Clauser pressure gradient parameter, defined as (Clauser 1954)

$$\beta = \frac{\delta^*}{\rho_w u_\tau^2} \frac{\mathrm{d}\bar{p}_w}{\mathrm{d}x}, \tag{3.4}$$

whose distribution along the symmetry axis is shown in figure 8(*c*). According to the DNS data, the flow field may be divided into five parts:

(i) ZPG1 for $x/\delta_{in} = 0$–39, where $\beta \approx 0$;
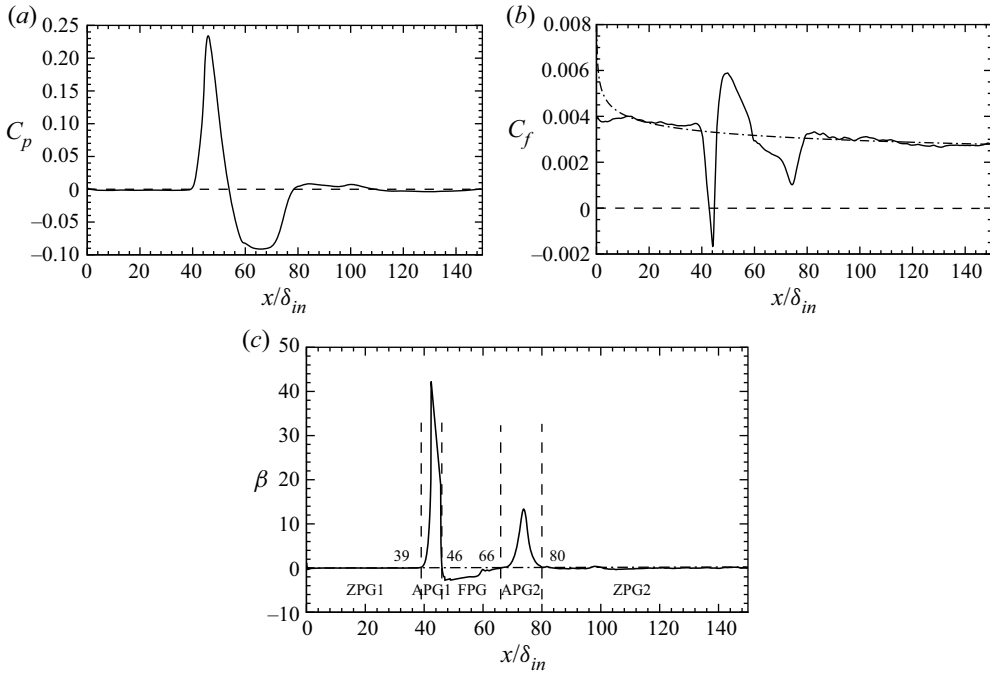
967 A3-12

Figure 8. Streamwise distributions of (*a*) pressure coefficient, (*b*) skin friction coefficient, and (*c*) Clauser pressure gradient parameter in the symmetry plane. The dash-dotted line in (*b*) represents (3.3).

(ii) APG1 for $x/\delta_{in} = 39$–46, where β exhibits a sharp positive peak;
(iii) FPG for $x/\delta_{in} = 46$–66, where β is negative as the flow accelerates;
(iv) APG2 for $x/\delta_{in} = 66$–80, where β attains a second positive peak;
(v)   ZPG2 for $x/\delta_{in} > 80$, where equilibrium conditions are recovered.

The mean velocity profiles across the interaction zone in the symmetry plane are reported in figure 9, for various streamwise stations. Before passing through the main interaction region, the velocity profiles do not show deviations with respect to canonical boundary layers. Moving downstream into the APG1 zone, the mean velocity profile shows negative values (station 4, $x/\delta_{in} = 44.0$), highlighted in the inset plot, denoting the presence of a turbulent separation bubble. Passing through the FPG region, the boundary layer tends to become thinner under the effects of the expansion. The opposite behaviour is observed in the APG2 region, where the boundary layer thickness increases again.

The structural modifications of turbulence statistics upon interaction with the conical shock wave are analysed here. In figure 10, we report the distributions of streamwise turbulence intensities at various streamwise stations on the symmetry plane. Upstream of the interaction zone, in the ZPG1 region, the profiles are again similar to each other, whereas in the mean separation region (station 4, at $x/\delta_{in} = 44.0$), the streamwise turbulence intensity increases, and attains its maximum value $u''_{rms}/u_e = 0.250$ at $y/\delta^*_{ref} = 0.51$ in the boundary layer. In the FPG region, considerations similar to those made for figure 9 about the effects of the expansion on the boundary layer thickness can be made, especially by looking at the wall-normal distance of the maximum of the u''_{rms} profile, with the maximum itself decreasing as well. In the APG2 region, the peak values increase
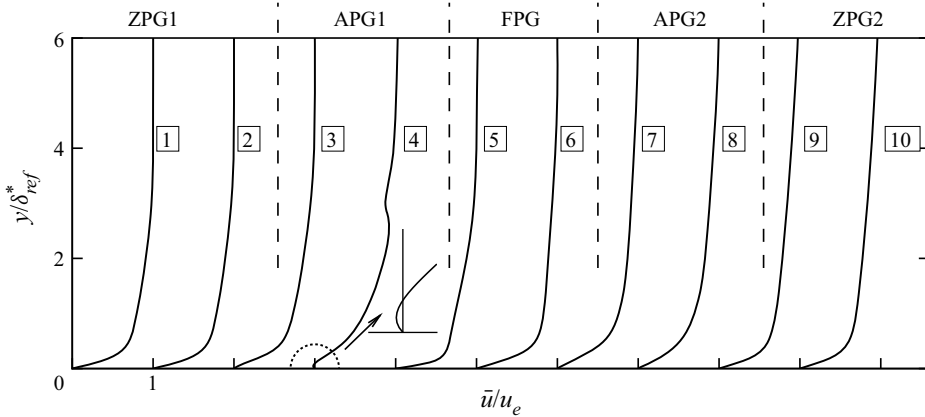
967 A3-13

Figure 9. Mean velocity profiles at the wall in the symmetry plane at various streamwise stations. The horizontal coordinate is $\bar{u}/u_e$, with $|\bar{u}/u_e| < 1$ inside the boundary layer. The vertical coordinate is y/δ^*_{ref}, where δ^*_{ref} is the boundary layer thickness at station 1. For nomenclature, refer to table 1.
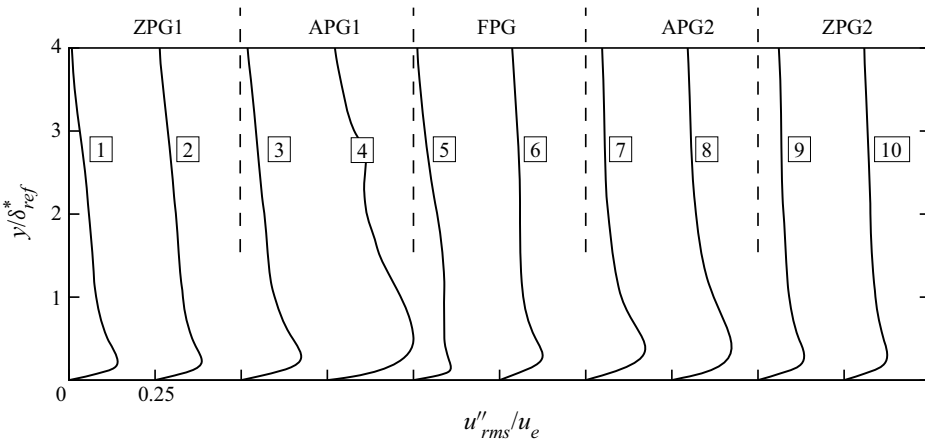

Figure 10. Streamwise turbulence intensities at various streamwise stations. The horizontal coordinate is u''_{rms}/u_e, in the range $0 < u''_{rms}/u_e < 0.25$. The vertical coordinate is y/δ^*_{ref}, where δ^*_{ref} is the boundary layer thickness at station 1. For nomenclature, refer to table 1.

again, assuming values below those obtained in the APG1 zone, with the peak value of the streamwise turbulence intensity $u''_{rms}/u_e = 0.173$ at $y/\delta^*_{ref} = 0.41$, for station 8.

4. Characterization of wall pressure fluctuations

4.1. *Pressure fluctuations distributions*

The wall pressure fluctuations are shown in figure 11, under different normalizations. Regardless of the normalization, the field looks noisy, due to lack of directions with spatial homogeneity for the averaging. However, the overall behaviour is quite clear: with exception of some common behaviour, such as rise of the magnitude in the interaction regions, with the highest values shown in the first interaction because of the flapping motion of the separation bubble (Priebe & Martin 2012), one can notice distinctly that
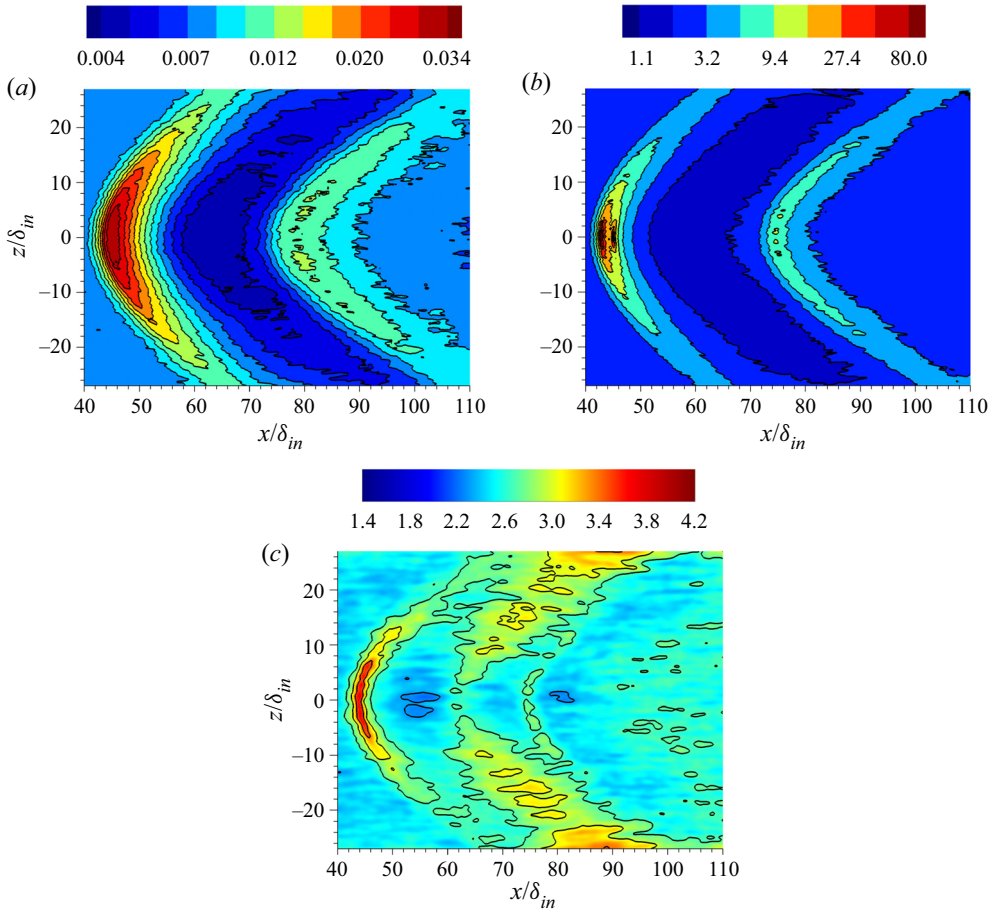
Figure 11. Pressure fluctuations at the wall with different normalizations: (*a*) scaled by free-stream dynamic pressure, $0.004 < p_{rms}/q_\infty < 0.034$, exponential distribution; (*b*) scaled by wall-surface shear stress, $1.1 < p_{rms}/|\tau_w| < 80$, exponential distribution; (*c*) scaled by local maximum Reynolds shear stress $\tau_m = \max_y(-\bar{\rho}\,\widetilde{u''v''})$, $1.4 < p_{rms}/\tau_m < 4.2$, linear distribution.

the pattern and the magnitude of p_{rms} are heavily dependent on the chosen normalization. When the free-stream dynamic pressure is used for normalization, large variations are observed between the upstream ZPG region and the APG and FPG regions. When the wall shear stress is used, large changes are observed close to the separation and reattachment zones, where the shear stress is close to zero. When the local maximum Reynolds shear stress within the boundary layer is used for normalization, the pressure fluctuations retain $O(1)$ amplitude throughout, with exception of the separation and reattachment lines.

For a more quantitative analysis, the data are now presented in the symmetry plane. Figure 12 shows r.m.s. pressure profiles in the wall-normal direction, up to $y/\delta_{in} = 4$, to exclude the wake region of the cone. In the ZPG regions (stations 1 and 10), the behaviour and the attained values are similar, but spread farther from the wall at station 10 owing to higher Reynolds number. In the APG region corresponding to the first interaction with separated flow (station 4), pressure fluctuations first increase slightly in a narrow region of the separated boundary layer to reach a plateau, then rise again up to a maximum, and finally decrease monotonically. The peak observed at station 4 corresponds to intersection
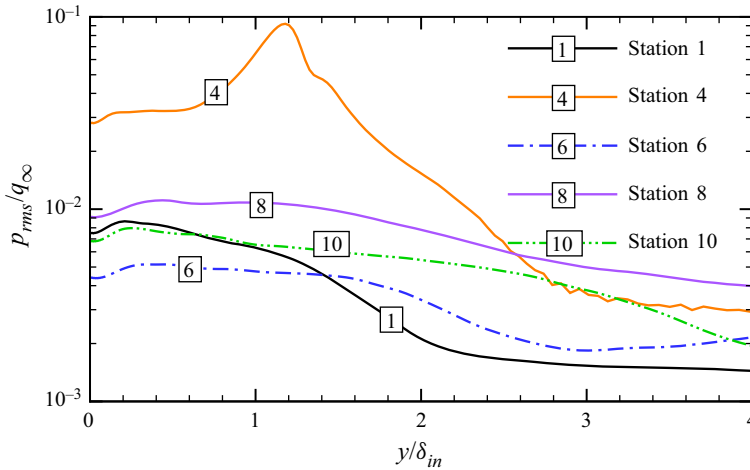
Figure 12. Profiles of r.m.s. pressure fluctuations at the streamwise stations 1, 4, 6, 8 and 10, scaled by the free-stream dynamic pressure q_∞. For nomenclature, refer to table 1.

with the reflected shock. Similar amplification of pressure fluctuations in the presence of a separated turbulent boundary layer was also reported by Na & Moin (1998) and Abe (2017). This behaviour is not observed at the other station representative of APG conditions (station 8), where separation does not occur. Very low pressure fluctuations are obtained in the FPG region (station 6), which is related to reduction of the number of vortical structures, as show in our previous work (Zuo *et al.* 2019).

The amplitude of the wall pressure fluctuations in the symmetry plane, as shown by the solid line in figure 13, is nearly constant in the incoming ZPG region, where $p_{rms} = 0.0072q_\infty$, corresponding to an overall sound pressure level ($p_{dB} = 20\log_{10}(p/(2\times10^{-5}\,\text{Pa}))$) of approximately 160.6 dB. In the same figure we also show the wall shear stress premultiplied by the factors 2.15 and 2.5. We find that for the incoming boundary layer, there is overlap between p_{rms} and $2.15\tau_w$, in agreement with the low-speed boundary layer DNS of Pirozzoli & Bernardini (2011*b*), who reported $p_{rms} = 2.2\tau_w$ for $Re_\tau \leq 250$, whereas in the second ZPG zone, we find $p_{rms} \approx 2.5\tau_w$, which again is in good agreement with what was obtained by Bernardini *et al.* (2011) ($p_{rms} = 2.5\tau_w$) and by Farabee & Casarella (1991) ($p_{rms} = 2.55\tau_w$) for $Re_\tau \leq 333$. As a note of caution, we point out that the value of p_{rms}/τ_w depends not only on Reynolds number, but also on the Mach number. Bernardini & Pirozzoli (2011) analysed supersonic adiabatic turbulent boundary layers at Mach numbers $M_\infty = 2, 3, 4$ by DNS, spanning a relatively large range of Reynolds numbers, namely $Re_\tau = 250–1100$. They found that at the wall, the value of p_{rms}/τ_w is affected mainly by Reynolds number variation, but increasing the Mach number also yields a slight increase. The range of values reported in that study is $p_{rms}/\tau_w = 2.2–2.8$, which is in good agreement with the present data. In the APG1 zone, the wall pressure fluctuations attain a maximum value $p_{rms} = 0.031q_\infty$, corresponding to an overall sound pressure level of approximately 173.3 dB. The minimum value is attained in the FPG zone where $p_{rms} \approx 0.0044q_\infty$, corresponding to an overall sound pressure level of approximately 156.3 dB. In the APG2 zone, a second local maximum $p_{rms} \approx 0.0115q_\infty$ is attained, corresponding to an overall sound pressure level of approximately 164.7 dB. The present DNS results in the separation
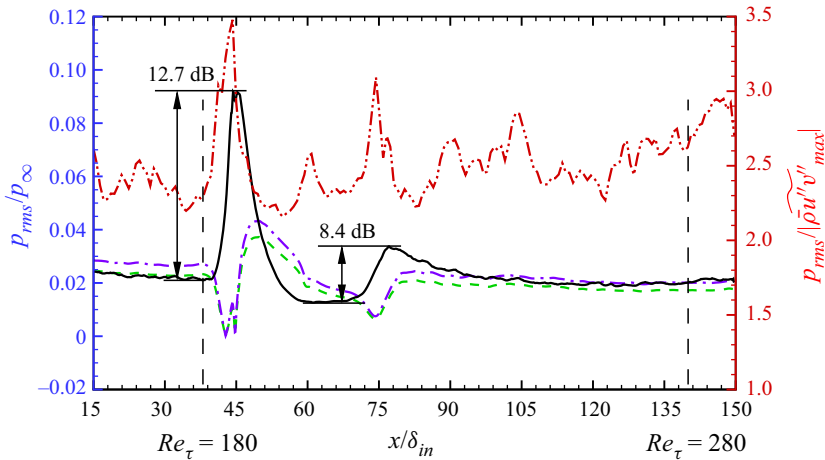
967 A3-16

Figure 13. Profile of p_{rms}/p_∞ (solid line), $2.15\tau_w$ (dashed line) and $2.5\tau_w$ (dash-dotted line), normalized by $\tau_m = \max_y(-\bar{\rho}\,\widetilde{u''v''})$ (dash-dot-dotted line). The vertical dashed lines denotes particular values of Re_τ.

region ($x/\delta_{in} = 43$–45) show a p_{rms} varying between 0.018 and 0.032, in good agreement with the Simpson *et al.* (1987) experimental data, in which the range is 0.020–0.031.

For completeness, figure 13 also shows the r.m.s. of wall pressure fluctuations in the symmetry plane, normalized by the local maximum Reynolds shear stress $-\bar{\rho}\,\widetilde{u''v''}_{max}$. In this case, a different scale is employed because of the different amplitudes involved. As observed by Simpson *et al.* (1987), the maximum Reynolds shear stress appears to be a better scale to normalize wall pressure fluctuations in separated turbulent boundary layers. With this scaling, the r.m.s. of wall pressure fluctuations in the experiments of Simpson *et al.* (1987) varied from 4.0 to 5.5 in the separation region. The present DNS results have normalized values between 2.5 and 4.0, i.e. somewhat less. However, Na & Moin (1998) also reported that the wall pressure fluctuations normalized by the local maximum Reynolds shear stress vary from 2.5 to 3.0 based on their DNS data ($Re_\theta = 670$, the same Reynolds number as our DNS at reference station), which is in good agreement with our results. As Na & Moin (1998) discussed, this sizeable difference may be explained as due to low-Reynolds-number effects. In fact, Choi & Moin (1990) compared available experimental and numerical data, and reported that variation of p_{rms} with the Reynolds numbers is rather large (p_{rms} at $Re_\theta = 13\,200$ is approximately 2.5 times that at $Re_\theta = 290$). Logarithmic growth of the pressure variance with Re_τ in canonical pipe flow has been reported recently by Yu, Ceci & Pirozzoli (2022). Considering the large difference in Reynolds numbers, the present results are compatible with the variation reported by Choi & Moin (1990).

4.2. *Frequency spectra*

Time series of wall pressure fluctuations in the symmetry plane at several different streamwise locations are reported in figure 14, which shows a wide range of time scales. Note that, as shown in figure 8(*b*), the boundary layer is separated at $x/\delta_{in} = 44$. To help the visualization, the vertical range is not the same in the various plots. As one moves towards the separation region, the frequency of the oscillations decreases noticeably, and the amplitude in the interaction zone increases significantly. Inside the separation region, the signal is dominated by low-frequency motions, as in the case of low-Reynolds-number
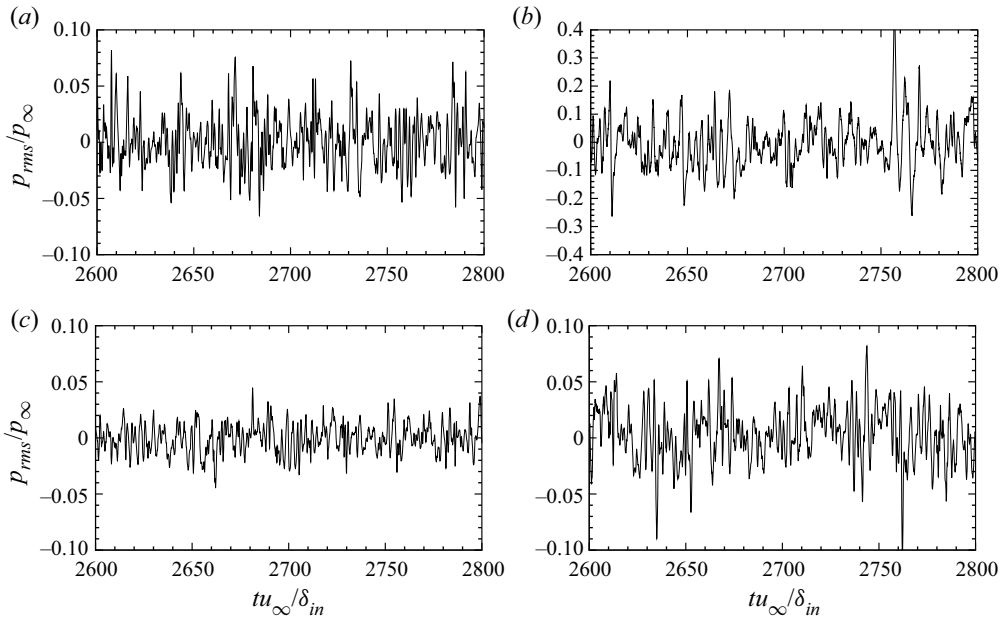
Figure 14. Time histories of wall pressure fluctuations in the symmetry plane. To facilitate visualization, the vertical ranges take different values: (*a*) $x/\delta_{in} = 27.5$, ZPG1 region; (*b*) $x/\delta_{in} = 44$, APG1 region; (*c*) $x/\delta_{in} = 62$, FPG region; (*d*) $x/\delta_{in} = 75$, APG2 region.

turbulent boundary layer separation (Na & Moin 1998). The long-time-scale behaviour noticed in figure 14(*b*) is associated with the movement of large-scale structures generated in the shear layer due to an inflectional hydrodynamic instability as in mixing layers. The signal in the second APG region (figure 14*d*) is again dominated by low-frequency motions; similar behaviour is observed in spanwise homogeneous compression ramp SBLI (Priebe & Martin 2012; Priebe *et al.* 2016) and other axisymmetric interactions (Estruch-Samper & Chandola 2018; Huang & Estruch-Samper 2018). The presence of low-frequency motions implies that a large statistical sample is required to get converged statistics inside the separation bubble. The amplitude of pressure fluctuation decreases in the FPG region (figure 14*c*), and the signal there is dominated by high-frequency motions again.

The PSD of the wall pressure signal (say, $E(f; x, y)$, where f is the frequency) has been estimated for locations ranging from the upstream flow to the downstream relaxation region, according to the Welch method, as suggested by Choi & Moin (1990) and Bernardini *et al.* (2011), hence subdividing the overall pressure record (covering a time span $140\delta_0^*/u_\infty$) into twelve overlapping segments. As shown by Bernardini *et al.* (2013), the frequency spectra of the wall pressure in wall-bounded flows obtained with finite-difference solvers may be contaminated from numerical dispersion errors. Hence frequencies higher than $0.1u_e/\delta^*$ are hereafter removed. The wall pressure spectrum for all numerical probes is shown in figure 15 as a function of both Strouhal numbers, $St_\delta = f\delta_{ref}/u_\infty$ and $St_L = fL/u_\infty$, with L the distance between the separation point and the nominal shock impingement location, and of the scaled streamwise coordinate x/δ_{in}. It should be noted that a premultiplied representation is used ($f E(f)$), such that equal areas yield equal contribution to the pressure variance when frequency is reported on a
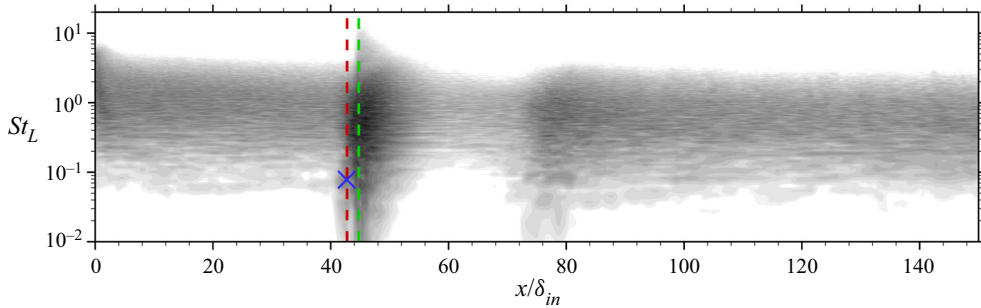
Figure 15. Contours of premultiplied PSD ($f E(f)$) of wall pressure fluctuations along the symmetry plane. The red line denotes the mean separation location, and the green line the mean reattachment location. The blue cross marks the position of the low-frequency peak near the separation line; $St_L = fL/u_\infty$ is the Strouhal number based on the interaction length scale.

logarithmic scale. Several regions can be identified, which are characterized by different characteristic time scales.

(i) A region dominated by high-frequency motions, $x/\delta_{in} < 40$, corresponding to the incoming turbulent boundary layer, with a peak at $St \approx 1$ associated with the energetic turbulent structures of the boundary layer (Gaitonde & Adler 2023). It should be emphasized that no significant energy was found in the range $0.01 < St_L < 0.1$ in the upstream boundary layer.

(ii) The zone around the foot of the reflected shock, $40 < x/\delta_{in} < 50$, which is characterized by strong low-frequency motions, especially near the separation point, and associated with flapping motion of the reflected shock system, similar to what is found in more canonical planar SBLIs (Dupont *et al.* 2006; Clemens & Narayanaswamy 2014). The PSD appears to be more broadbanded, and its peak is clearly shifted to lower frequencies due to the thickening of the boundary layer. A limited part of the broadband energy in the premultiplied spectra is found close to the foot of the reflected shock at frequencies that are two orders of magnitude lower than the turbulent structures of the incoming boundary layer.

(iii) The FPG zone, $50 < x/\delta_{in} < 65$, in which low and intermediate scales are dominant, whose frequencies range between the low ones typical of the shock motion and the high ones associated with the incoming turbulence.

(iv) The secondary interaction zone, $65 < x/\delta_{in} < 80$, which shows the same behaviour as zone (ii), hence characterized by frequencies that are 1–2 orders of magnitude less than the turbulent structures of the incoming boundary layer.

(v) A relaxation zone, $x/\delta_{in} > 80$, where the high-frequency motions developing inside the interaction zones become dominant again as the boundary layer returns to an equilibrium state.

In this respect, we note that in spanwise homogeneous SBLIs, typical low-frequency oscillations arising around the separation point have a typical frequency $St_L \approx 0.03$, hence two orders of magnitude less than the dominant frequencies in the boundary layer. Experiments and numerical studies of SBLIs in the presence of flow skewing, including compression ramps (Erengil & Dolling 1993; Vanstone *et al.* 2017; Adler & Gaitonde 2018, 2020), sharp fins (Schmisseur & Dolling 1994; Gaitonde *et al.* 1999; Arora, Mears & Alvi 2019) and swept impinging oblique SBLIs (Doehrmann *et al.* 2018;
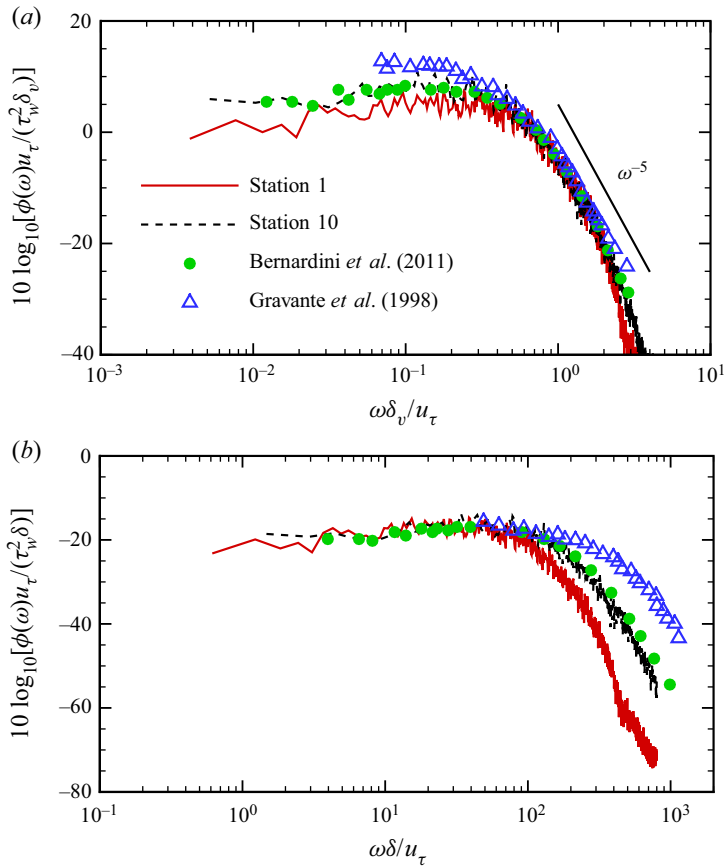
Figure 16. Wall pressure frequency spectrum in ZPG regions. Station 1 is at Reynolds number $Re_\tau = 160$. Station 10 is at Reynolds number $Re_\tau = 280$, at flow conditions comparable with Bernardini *et al.* (2011) at $Re_\tau = 340$ (green solid circles) and Gravante *et al.* (1998) at $Re_\tau = 715$ (blue open triangles). Pressure is scaled with respect to τ_w^2, and the reference time is δ_v/u_τ in (*a*) and δ/u_τ in (*b*).

Padmanabhan *et al.* 2021), rather seem to indicate suppression of the low-frequency peak in the presence of 3-D effects, on account of a topological change of the separation bubble from a closed to an open type. Recently, Ceci *et al.* (2023) have proposed that the typical frequencies increase with the skew angle, on account of propagation spanwise travelling disturbances. Figure 15 shows evidence for 2-D-like dynamics in the proximity of the separation and reattachment points, as well as in the secondary APG region. This is the likely consequence that the dynamics in the symmetry plane is similar to nominally 2-D interactions.

To analyse the pressure spectra in greater detail, a comparison in the ZPG region with well-established results is reported in figure 16. The shapes of the frequency spectra at stations 1 and 10, corresponding to ZPG conditions, adopting two different normalizations, conform in general terms to those observed in low-speed boundary layers. In figure 16(*a*), pressure is scaled with respect to τ_w^2 and the reference time is δ_v/u_τ. In figure 16(*b*), the mixed time scale δ/u_τ is used instead. Good collapse with the experimental data of Gravante *et al.* (1998) and previous DNS database of Bernardini *et al.* (2011) at comparable friction Reynolds number with respect to station 10, is observed in the middle- and
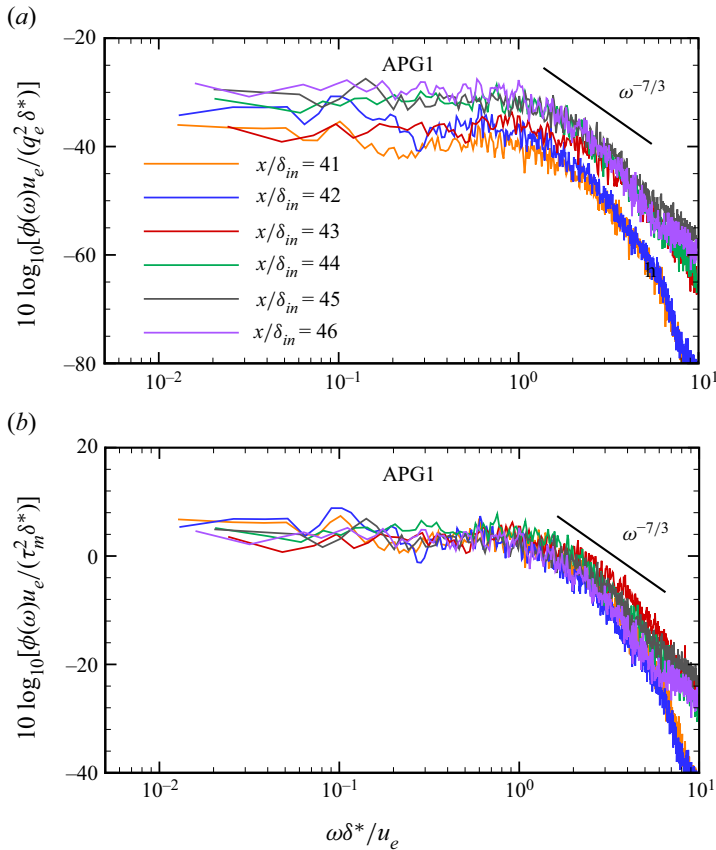
Figure 17. Frequency spectra of the wall pressure at various stations in the APG1 region. Local outer scaling is used, and pressure is scaled by (*a*) q_e^2 or (*b*) τ_m^2. Data are taken at $x/\delta_{in} = 41, 42, 43, 44, 45, 46$.

high-frequency end of the spectrum, which is dominated by the influence of near-wall motions (Blake 2017), when pressure is scaled with respect to the wall friction, and viscous time units are used for normalizations. The use of a 'mixed' time scale (δ/u_τ), which is expected to yield better collapse of the low-/intermediate-frequency end of the spectrum, still yields a satisfactory comparison with the experimental data of Gravante *et al.* (1998). As predicted theoretically by Blake (2017), the spectrum approximately drops off as ω^{-5} at high frequencies. In this range of scales, inner scaling leads to good collapse between different Reynolds numbers, which is lost with use of the mixed time scale. The low-frequency ω^2 scaling, reported in an experiment for incompressible turbulent boundary layer by Farabee & Casarella (1991), is not observed here, possibly because of limited duration of the time sample. Overall, the agreement between the spectrum at station 10 with reference data is excellent, which corroborates the quality of present results.

The wall frequency spectra in the APG1 regions are reported in figure 17, under condition of boundary layer separation. To verify the possible occurrence of universal scaling laws, the spectra are now normalized with respect to either the local external dynamic pressure q_e, or the local maximum shear stress τ_m. In both cases, the local (outer) reference time δ^*/u_e is adopted. The latter scaling is expected to partially account for non-equilibrium effects caused by the APG (Mabey 1982), as indeed is verified by
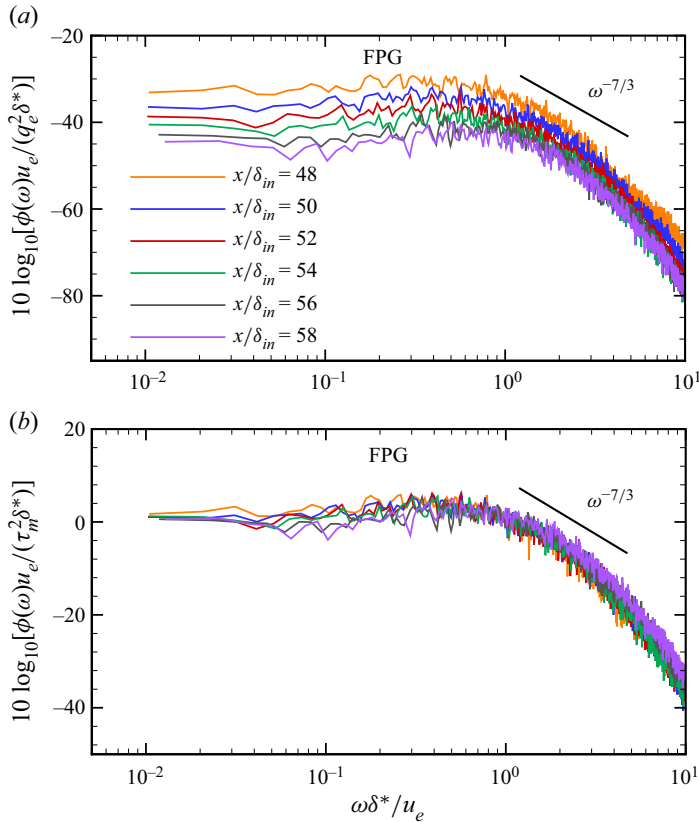
Figure 18. Frequency spectra of the wall pressure at various stations in the FPG region. Local outer scaling is used, and pressure is scaled by (a) q_e^2 or (b) τ_m^2. Data are taken at $x/\delta_{in} = 48, 50, 52, 54, 56, 58$.

Simpson *et al.* (1987) and Na & Moin (1998). The shape of pressure spectra in the APG1 region is similar to that observed in the ZPG regions. Reasonable universality is achieved when pressure is scaled with respect to τ_m, especially at low and middle frequencies, whereas at high frequencies, significant scatter is observed, maybe caused by turbulent boundary layer separation ($x/\delta_{in} = 44$–45). On the other hand, when pressure is normalized by q_∞, an increase of the PSD progressing in the streamwise direction is observed at all frequencies, as also reported by Na & Moin (1998) and Bernardini *et al.* (2011). This indicates that the free-stream dynamic pressure has less direct influence on the wall pressure spectra than the local maximum shear stress inside the separation bubble.

The spectra downstream of the reattachment point in the FPG region are reported in figure 18. Similar to the observation made for the APG1 region, reasonable universality is obtained when pressure is scaled with respect to τ_m at low and middle frequencies. It should be noted that when pressure is normalized by q_e, a decrement of the PSD progressing in the streamwise direction is observed at all frequencies. This is the opposite behaviour with respect to the APG1 regions, indicating that the pressure gradient has a strong effect on the power spectra of wall pressure fluctuations.

The frequency spectra in the APG2 region without turbulent separation are shown in figure 19. The data nearly collapse to a single distribution regardless of the normalization
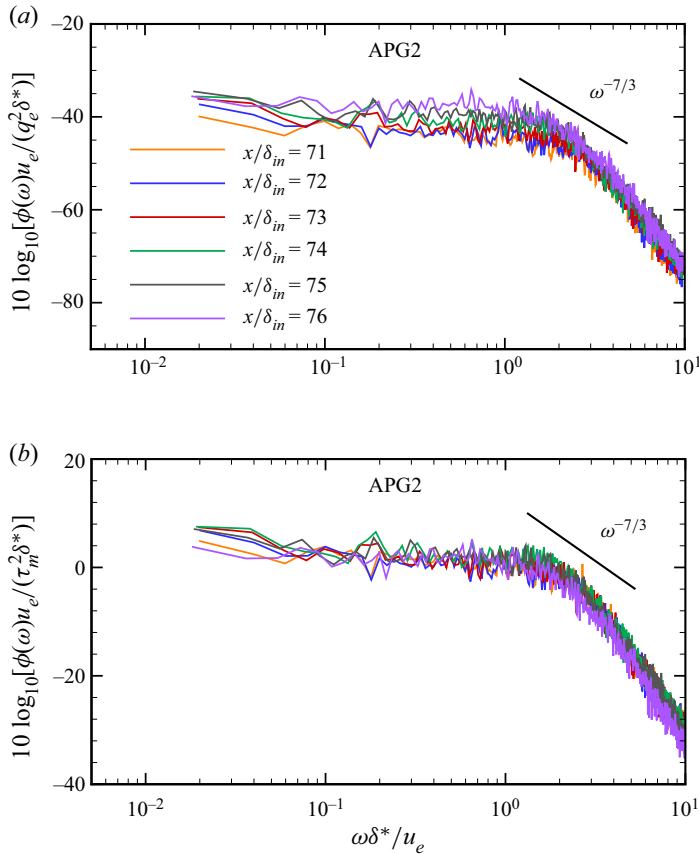
967 A3-22

Figure 19. Frequency spectra of the wall pressure at various stations in the APG2 region. Local outer scaling is used, and pressure is scaled by (*a*) q_e^2 or (*b*) τ_m^2. Data are taken at $x/\delta_{in} = 71, 72, 73, 74, 75, 76$.

at all frequencies, indicating that the wall pressure field has recovered past the separation. Actually, self-similar structure of the boundary layer was also found in our previous study (Zuo *et al.* 2019).

4.3. *Two-point correlations*

The spatial imprinting of pressure fluctuations at the wall is investigated in this subsection through the analysis of the two-point space–time correlation coefficient, defined as

$$R_{pp}(x; r_1, r_2, r_3, \tau) = \frac{\langle p'(x, 0, z, t)\, p'(x + r_1, r_2, z + r_3, t + \tau)\rangle}{p_{rms}(x, 0)\, p_{rms}(x + r_1, r_2)}, \qquad (4.1)$$

where (r_1, r_2, r_3) is the spatial separation vector, and τ is the time delay.

Iso-lines of the two-point spatial correlation in the wall plane $R_{pp}(x; r_1, 0, r_3, 0)$ are displayed at various stations in figure 20. Differences among the various flows are visible, the dominant effect being due to the pressure gradient. In the ZPG region (station 1), the contours of R_{pp} are roughly circular at small separations, indicating near-isotropy of the pressure-carrying eddies (Probsting *et al.* 2013). At larger separations in the APG1 region, the iso-lines become more elongated in the spanwise direction, reflecting an anisotropic state of the large structures. In the APG1 region (mean flow separation), an increase of the characteristic pressure length scales is observed, and the iso-lines become more elongated
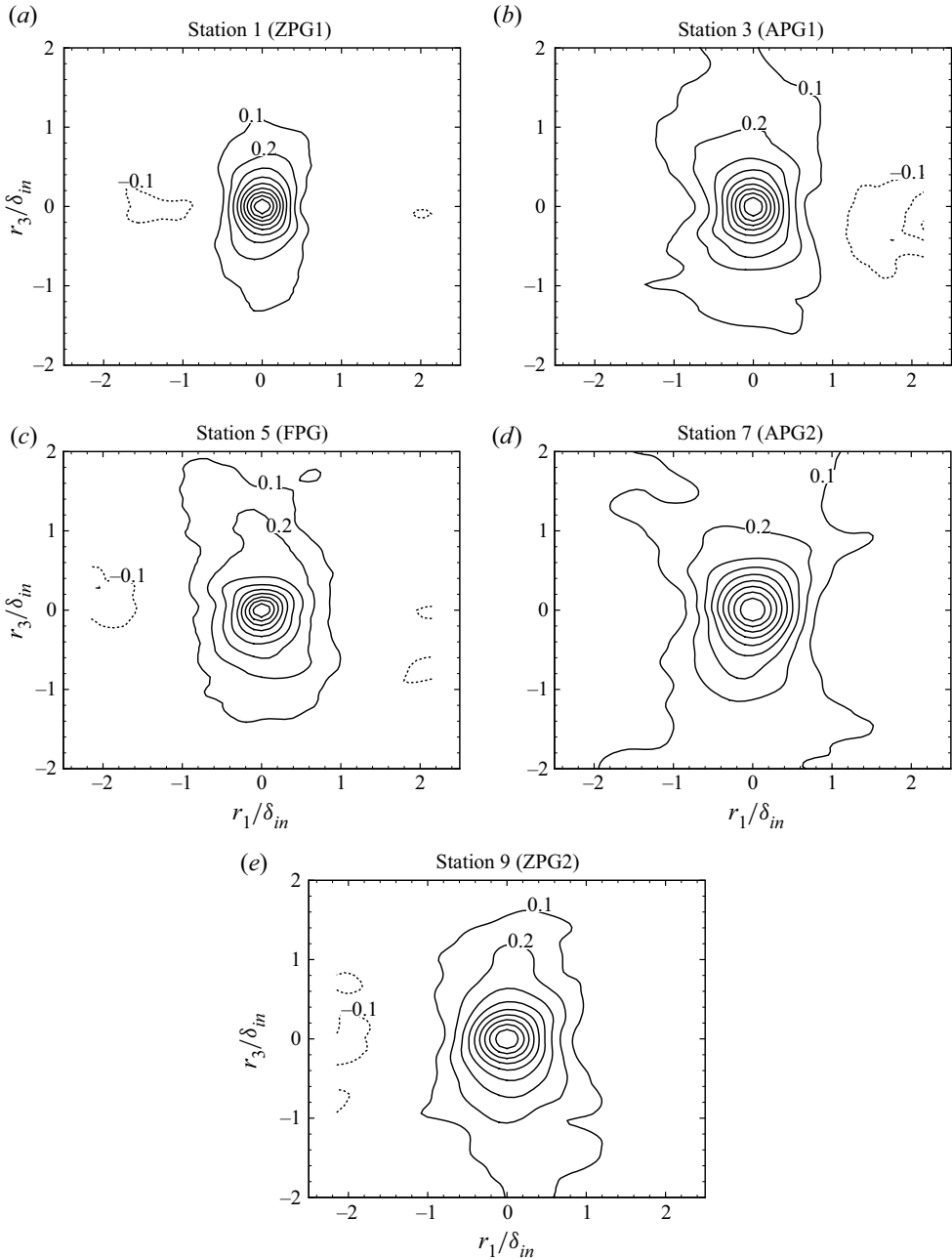
Figure 20. Iso-lines of two-point pressure correlation $R_{pp}(x; r_1, 0, r_3, 0)$ at streamwise stations 1, 3, 5, 7 and 9 in (*a–d*), respectively, are shown. Ten equally spaced contour levels are shown, from -0.1 to 0.9 (the zero iso-line is omitted).

in the spanwise direction. Downstream of the bubble (station 3), where the flow field redevelops under strong FPG, the flow begins to recover. The shapes of iso-lines slowly revert back to those of attached boundary layers. However, the iso-lines is still elongated to a certain extent in the spanwise direction. In the APG2 region (instantaneous flow
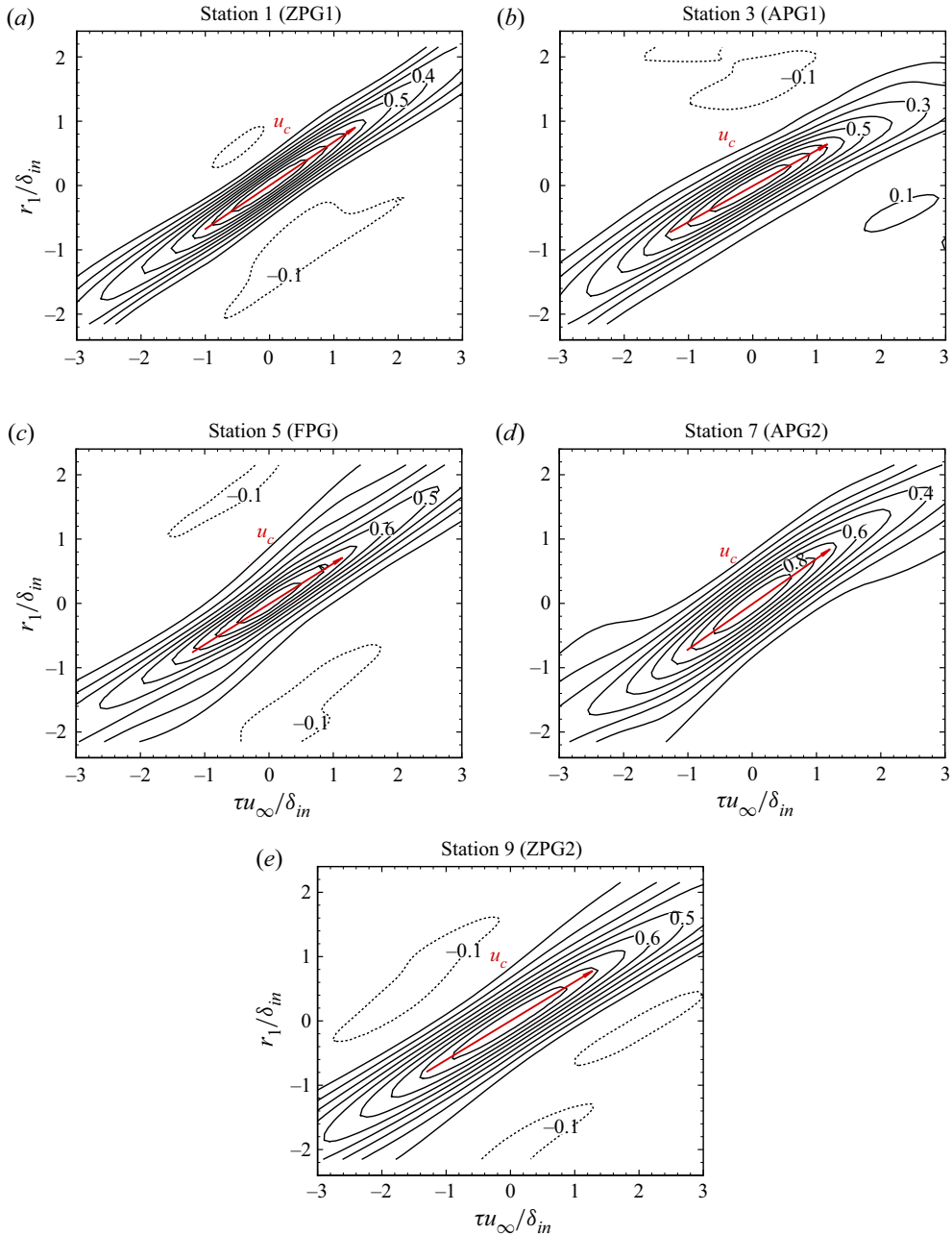
Figure 21. (*a–e*) Iso-lines of the space–time correlation $R_{pp}(x; r_1, 0, 0, \tau)$ at streamwise stations 1, 3, 5, 7 and 9, respectively. Ten equally spaced contour levels are shown, from -0.1 to 0.9 (the zero iso-line is omitted). The slope of the red line represents the magnitude of convection velocity.

reversal), an elongated two-point correlation in the spanwise direction is again observed. In the ZPG2 region, the boundary layer returns to an equilibrium state Zuo *et al.* (2019), and the spatial coherence of the pressure field begins to decrease consistently. However, spatial coherences of ZPG1 and ZPG2 differ slightly, due mainly to the effect of the different Re_τ.

	Station 1	Station 3	Station 5	Station 7	Station 9
Region	ZPG1	APG1	FPG	APG2	ZPG2
U_c/U_∞	0.678	0.558	0.628	0.706	0.607

Table 2. Local convection velocity of wall pressure fluctuations at different locations, normalized by local free-stream velocity U_∞.

As proven by Bernardini & Pirozzoli (2011), as Re_τ increases, the spatial coherence of the pressure field is found to decrease.

4.4. *Space–time correlations*

Contour lines of the space–time correlation coefficient $R_{pp}(x; r_1, 0, 0, \tau)$ are shown in figure 21, including lines with slope equal to the convection velocity U_c. Proceeding as in Bernardini & Pirozzoli (2011), we define the convection velocity corresponding to a given time delay τ as the ratio r_1/τ taken at the value of r_1 where a local maximum is attained. The convection velocities obtained at different stations are reported in table 2. As for the two-point spatial correlations, the shape of the maps reflects the convective nature of the pressure field, which is characterized by coherent downstream propagation of pressure-carrying eddies. The space–time organization of the pressure field upstream of the interaction is similar to that observed in the ZPG compressible boundary layer (Bernardini & Pirozzoli 2011; Duan, Choudhari & Zhang 2016).

The convection velocities of wall pressure fluctuations decrease as the pressure gradient increases. When in the FPG region, the convection velocity shows an increasing trend, consistently with the results of Na & Moin (1998) and Bernardini & Pirozzoli (2011), whereas coherence tends to decrease while progressing downstream, as seen by the increased spreading of the contour lines, which is most apparent in the separated (APG1) region.

From the maps of figure 21, one can deduce the characteristic convection velocities (U_c) of the eddies. The convection speed of the large-scale disturbances is associated with low frequencies (Na & Moin 1998; Bernardini *et al.* 2011). When data are scaled with respect to the free-stream velocity (U_∞), pressure disturbances are found to propagate at speeds in the range $0.6U_\infty$–$0.7U_\infty$. Such behaviour is consistent with the results of Schloemer (1967), Na & Moin (1998) and Bernardini *et al.* (2011), who found that, compared with the canonical boundary layer case, the convection velocities are higher under FPG and lower under APG.

5. Conclusions

The pressure signature of a conical shock wave/boundary layer interaction has been investigated exploiting a numerical database provided by direct simulation of the Navier–Stokes equations. In the first adverse pressure gradient zone (APG1), the boundary layer undergoes separation and reattachment with a turbulent separation bubble. The second adverse pressure gradient (zone APG2) is mild, and the boundary layer remains attached.

The analysis has shown that pressure fluctuations are strongly amplified across the interaction, and the maximum amplification occurs in the APG1 region past the incident conical shock. At the wall, the r.m.s. wall pressure fluctuations attain a very large value

(in excess of 173.3 dB), with a maximum increase of approximately 12.7 dB from the incoming level. In the APG2 region, they attain a second large value (approximately 164.7 dB), with an increase of approximately 8.4 dB from the upstream level.

The wall pressure power spectral density exhibits a broadband and energetic low-frequency component associated with the separation-conical-shock unsteadiness. The field can be separated into five principal zones, each involving characteristic temporal scales. A limited part of the broadband energy in the premultiplied spectra is found close to the foot of the reflected conical shock, at frequencies two orders of magnitude lower than the typical turbulent structures of the incoming boundary layer.

The shape of the wall pressure frequency spectra is modified qualitatively by the interaction with the conical shock wave, and different Fourier modes under different pressure gradients have been identified. Behaviour of frequency spectra in favourable pressure gradient is observed to be opposite to that in APG regions, when pressure is normalized by free-stream dynamic pressure. Inside the separation bubble, the frequency spectra of wall pressure fluctuations normalized by the local maximum Reynolds shear stress yield better universality than those normalized by free-stream dynamic pressure, indicating that local Reynolds shear stress has more direct influence on the wall pressure spectra, whereas in the APG without separation, the data collapse reasonably to a single distribution regardless of the normalization at all frequencies, indicating that the wall pressure field has been recovered from separation.

The space–time wall pressure correlations reveal an increase of the characteristic length scales associated with the pressure field and a strong reduction of the convection velocities in the APG region. Contour plots of two-point correlation of wall pressure fluctuations in the streamwise–spanwise plane are highly elongated in the spanwise direction inside the separation bubble, implying the presence of large 2-D roller-type structures. The convection velocity determined from the space–time correlation of pressure fluctuations is as low as $0.558U_\infty$ in the separated APG1 zone, and increases downstream of the FPG region.

Author ORCIDs.
- Feng-Yuan Zuo https://orcid.org/0000-0003-4742-0240;
- Antonio Memmolo https://orcid.org/0000-0002-4066-9740;
- Sergio Pirozzoli https://orcid.org/0000-0002-7160-3023.

REFERENCES

ABE, H. 2017 Reynolds-number dependence of wall-pressure fluctuations in a pressure-induced turbulent separation bubble. *J. Fluid Mech.* **833**, 563–598.

ADAMS, N.A. 2000 Direct simulation of the turbulent boundary layer along a compression ramp at $M = 3$ and $Re_\theta = 1685$. *J. Fluid Mech.* **420**, 47–83.

ADLER, M.C. & GAITONDE, D.V. 2018 Unsteadiness in shock/turbulent-boundary-layer interactions with open flow separation. *2018 AIAA Aerospace Sciences Meeting*. AIAA Paper 2018-2075. American Institute of Aeronautics and Astronautics.

ADLER, M.C. & GAITONDE, D.V. 2020 Dynamics of strong swept-shock/turbulent-boundary-layer interactions. *J. Fluid Mech.* **896**, A29.

ADLER, M.C. & GAITONDE, D.V. 2022 Influence of separation structure on the dynamics of shock/turbulent-boundary-layer interactions. *Theor. Comput. Fluid Dyn* **36**, 303–326.

ARORA, N., MEARS, L. & ALVI, F.S. 2019 Unsteady characteristics of a swept-shock/boundary-layer interaction at Mach 2. *AIAA J.* **57**, 4548–4559.

BERNARDINI, M., MODESTI, D. & PIROZZOLI, S. 2016 On the suitability of the immersed boundary method for the simulation of high-Reynolds-number separated turbulent flows. *Comput. Fluids* **130**, 84–93.

BERNARDINI, M. & PIROZZOLI, S. 2011 Wall pressure fluctuations beneath supersonic turbulent boundary layers. *Phys. Fluids* **23**, 085102.

BERNARDINI, M., PIROZZOLI, S. & GRASSO, F. 2011 The wall pressure signature of transonic shock/boundary layer interaction. *J. Fluid Mech.* **671**, 288–312.

BERNARDINI, M., PIROZZOLI, S., QUADRIO, M. & ORLANDI, P. 2013 Turbulent channel flow simulations in convecting reference frames. *J. Comput. Phys.* **232**, 1–6.

BLAKE, W.K. 2017 *Mechanics of Flow-induced Sound and Vibration, Volume 2: Complex Flow–Structure Interactions*. Academic.

BURTON, D.M.F. & BABINSKY, H. 2012 Corner separation effects for normal shock wave/turbulent boundary layer interactions in rectangular channels. *J. Fluid Mech.* **707**, 287–306.

CAMUSSI, R., GUJ, G., IMPERATORE, B., PIZZICAROLI, A. & PERIGO, D. 2007 Wall pressure fluctuations induced by transonic boundary layers on a launcher model. *Aerosp. Sci. Technol.* **11** (5), 349–359.

CEBRAL, J.R. & LOHNER, R. 1997 Conservative load projection and tracking for fluid–structure problems. *AIAA J.* **35** (4), 687–692.

CECI, A., PALUMBO, A., LARSSON, J. & PIROZZOLI, S. 2023 On low-frequency unsteadiness in swept shock wave–boundary layer interactions. *J. Fluid Mech.* **956**, R1.

CHOI, H. & MOIN, P. 1990 On the space–time characteristics of wall-pressure fluctuations. *Phys. Fluids* **2** (8), 1450–1460.

CLAUSER, F.H. 1954 Turbulent boundary layers in adverse pressure gradients. *J. Aeronaut. Sci.* **21** (2), 91–108.

CLEMENS, N.T. & NARAYANASWAMY, V. 2014 Low-frequency unsteadiness of shock wave/turbulent boundary layer interactions. *Annu. Rev. Fluid Mech.* **46**, 469–492.

DOEHRMANN, A.C., PADMANABHAN, S., THREADGILL, J.A. & LITTLE, J.C. 2018 Effect of sweep on the mean and unsteady structures of impinging shock/boundary layer interactions. *2018 AIAA Aerospace Sciences Meeting*. AIAA Paper 2018-2074. American Institute of Aeronautics and Astronautics.

DOLLING, D.S. 2001 Fifty years of shock-wave/boundary-layer interaction research: what next? *AIAA J.* **39** (8), 1517–1531.

DUAN, L., CHOUDHARI, M.M. & ZHANG, C. 2016 Pressure fluctuations induced by a hypersonic turbulent boundary layer. *J. Fluid Mech.* **804**, 578–607.

DUPONT, P., HADDAD, C. & DEBIEVE, J.F. 2006 Space and time organization in a shock-induced separated boundary layer. *J. Fluid Mech.* **559**, 255–277.

DUPONT, P., PIPONNIAU, S. & DUSSAUGE, J.P. 2019 Compressible mixing layer in shock-induced separation. *J. Fluid Mech.* **863**, 620–643.

ERENGIL, M.E. & DOLLING, D.S. 1993 Effects of sweepback on unsteady separation in Mach 5 compression ramp interactions. *AIAA J.* **31**, 302–311.

ESTRUCH-SAMPER, D. & CHANDOLA, G. 2018 Separated shear layer effect on shock-wave/turbulent-boundary-layer interaction unsteadiness. *J. Fluid Mech.* **848**, 154–192.

EXPOSITO, D., GAI, S.L. & NEELY, A.J. 2021 Wall temperature and bluntness effects on hypersonic laminar separation at a compression corner. *J. Fluid Mech.* **922**, A1.

FADLUN, E.A., VERZICCO, R., ORLANDI, P. & MOHD-YUSOF, J. 2000 Combined immersed-boundary finite-difference methods for three-dimensional complex flow simulations. *J. Comput. Phys.* **161** (1), 35–60.

FARABEE, T.M. & CASARELLA, M.J. 1991 Spectral features of wall pressure fluctuations beneath turbulent boundary layers. *Phys. Fluids* A*: Fluid* **3** (10), 2410–2420.

GAI, S.L. & TEH, S.L. 2000 Interaction between a conical shock wave and a plane turbulent boundary layer. *AIAA J.* **38** (5), 804–811.

GAITONDE, D.V. & ADLER, M.C. 2023 Dynamics of three-dimensional shock-wave/boundary-layer interactions. *Annu. Rev. Fluid Mech.* **55**, 291–321.

GAITONDE, D.V., SHANG, J.S., GARRISON, T.J., ZHELTOVODOV, A.A. & MAKSIMOV, A.I. 1999 Three-dimensional turbulent interactions caused by asymmetric crossing-shock configurations. *AIAA J.* **37**, 1602–1608.

GANAPATHISUBRAMANI, B., CLEMENS, N.T. & DOLLING, D.S. 2007 Effects of upstream boundary layer on the unsteadiness of shock-induced separation. *J. Fluid Mech.* **585**, 369–394.

GRAVANTE, S.P., NAGUIB, A.M., WARK, C.E. & NAGIB, H.M. 1998 Characterization of the pressure fluctuations under a fully developed turbulent boundary layer. *AIAA J.* **36** (10), 1808–1816.

HALE, J. 2015 Interaction between a conical shock wave and a plane compressible turbulent boundary layer at Mach 2.05. PhD thesis, University of Illinois at Urbana-Champaign, Champaign, IL.

HELM, C.M., MARTIN, M.P. & WILLIAMS, O.J.H. 2021 Characterization of the shear layer in separated shock/turbulent boundary layer interactions. *J. Fluid Mech.* **912**, A7.

HUANG, X. & ESTRUCH-SAMPER, D. 2018 Low-frequency unsteadiness of swept shock-wave/turbulent-boundary-layer interaction. *J. Fluid Mech.* **856**, 797–821.

HUMBLE, R.A., ELSINGA, G.E., SCARANO, F. & VAN OUDHEUSDEN, B.W. 2009 Three-dimensional instantaneous structure of a shock wave/turbulent boundary layer interaction. *J. Fluid Mech.* **622**, 33–62.

JI, M. & WANG, M. 2012 Surface pressure fluctuations on steps immersed in turbulent boundary layers. *J. Fluid Mech.* **712**, 471–504.

KARNICK, P.T. & VENKATRAMAN, K. 2017 Shock–boundary layer interaction and energetics in transonic flutter. *J. Fluid Mech.* **832**, 212–240.

KIYA, M. & SASAKI, K. 1983 Structure of a turbulent separation bubble. *J. Fluid Mech.* **137**, 83–113.

LUSHER, D.J. & SANDHAM, N.D. 2020 The effect of flow confinement on laminar shock-wave/boundary-layer interactions. *J. Fluid Mech.* **897**, A18.

MABEY, D.G. 1972 Analysis and correlation of data on pressure fluctuations in separated flow. *J. Aircraft* **9** (9), 642–645.

MABEY, D.G. 1982 Comment on 'A review of research on subsonic turbulent flow attachment'. *AIAA J.* **20** (11), 1632.

MARTELLI, E., CIOTTOLI, P.P., BERNARDINI, M., NASUTI, F. & VALORANI, M. 2017 Detached-eddy simulation of shock unsteadiness in an overexpanded planar nozzle. *AIAA J.* **55** (6), 2016–2028.

MOHAMMED, T.A. & WEISS, J. 2016 Unsteadiness in a large turbulent separation bubble. *J. Fluid Mech.* **799**, 383–412.

MORGAN, B., DURAISAMY, K., NGUYEN, N., KAWAI, S. & LELE, S.K. 2013 Flow physics and RANS modelling of oblique shock/turbulent boundary layer interaction. *J. Fluid Mech.* **729**, 231–284.

NA, Y. & MOIN, P. 1998 The structure of wall-pressure fluctuations in turbulent boundary layers with adverse pressure gradient and separation. *J. Fluid Mech.* **377**, 347–373.

O'ROURKE, J. 1998 *Computational Geometry in C*. Cambridge University Press.

PADMANABHAN, S., MALDONADO, J.C., THREADGILL, J.A.S. & LITTLE, J.C. 2021 Experimental study of swept impinging oblique shock/boundary-layer interactions. *AIAA J.* **59** (1), 140–149.

PASQUARIELLO, V., HICKEL, S. & ADAMS, N.A. 2017 Unsteady effects of strong shock-wave/boundary-layer interaction at high Reynolds number. *J. Fluid Mech.* **823**, 617–657.

PIPONNIAU, S., DUSSAUGE, J.P., DEBIEVE, J.F. & DUPONT, P. 2009 A simple model for low-frequency unsteadiness in shock-induced separation. *J. Fluid Mech.* **629**, 87–108.

PIROZZOLI, S. 2010 Generalized conservative approximations of split convective derivative operators. *J. Comput. Phys.* **229** (19), 7180–7190.

PIROZZOLI, S. 2011 Numerical methods for high-speed flows. *Annu. Rev. Fluid Mech.* **43**, 163–194.

PIROZZOLI, S. & BERNARDINI, M. 2011*a* Direct numerical simulation database for impinging shock wave/turbulent boundary-layer interaction. *AIAA J.* **49** (6), 1307–1312.

PIROZZOLI, S. & BERNARDINI, M. 2011*b* Turbulence in supersonic boundary layers at moderate Reynolds number. *J. Fluid Mech.* **688**, 120–168.

PIROZZOLI, S., BERNARDINI, M. & GRASSO, F. 2010 Direct numerical simulation of transonic shock/boundary layer interaction under conditions of incipient separation. *J. Fluid Mech.* **657**, 361–393.

POINSOT, T.J. & LELE, S.K. 1992 Boundary conditions for direct simulations of compressible viscous flows. *J. Comput. Phys.* **101** (1), 104–129.

PRIEBE, S. & MARTIN, M.P. 2012 Low-frequency unsteadiness in shock wave–turbulent boundary layer interaction. *J. Fluid Mech.* **699**, 1–49.

PRIEBE, S., TU, J.H., ROWLEY, C.W. & MARTIN, M.P. 2016 Low-frequency dynamics in a shock-induced separated flow. *J. Fluid Mech.* **807**, 441–477.

PROBSTING, S., SCARANO, F., BERNARDINI, M. & PIROZZOLI, S. 2013 On the estimation of wall pressure coherence using time-resolved tomographic PIV. *Exp. Fluids* **54**, 1567.

ROBINET, J.C. 2007 Bifurcations in shock-wave/laminar-boundary-layer interaction: global instability approach. *J. Fluid Mech.* **579**, 85–112.

SANDHAM, N.D., SCHUELEIN, E., WAGNER, A., WILLEMS, S. & STEELANT, J. 2014 Transitional shock-wave/boundary-layer interactions in hypersonic flow. *J. Fluid Mech.* **752**, 349–382.

SARTOR, F., METTOT, C., BUR, R. & SIPP, D. 2015 Unsteadiness in transonic shock-wave/boundary-layer interactions: experimental investigation and global stability analysis. *J. Fluid Mech.* **781**, 550–577.

SCHLOEMER, H.H. 1967 Effects of pressure gradients on turbulent-boundary-layer wall-pressure fluctuations. *J. Acoust. Soc. Am.* **42** (1), 93–113.

SCHMISSEUR, J.D. & DOLLING, D.S. 1994 Fluctuating wall pressures near separation in highly swept turbulent interactions. *AIAA J.* **32**, 1151–1157.

SIMPSON, R.L., GHODBANE, M. & MCGRATH, B.E. 1987 Surface pressure fluctuations in a separating turbulent boundary layer. *J. Fluid Mech.* **177**, 167–186.

SMITS, A.J. & DUSSAUGE, J.P. 2006 *Turbulent Shear Layers in Supersonic Flow*. Springer.

TESSICINI, F., IACCARINO, G., FATICA, M., WANG, M. & VERZICCO, R. 2002 Wall modeling for large-eddy simulation using an immersed boundary method. In *Annual Research Briefs, Stanford University Center for Turbulence Research, Stanford, CA*, pp. 181–187.

TOUBER, E. & SANDHAM, N.D. 2011 Low-order stochastic modelling of low-frequency motions in reflected shock-wave/boundary-layer interactions. *J. Fluid Mech.* **671**, 417–465.

VANSTONE, L., SALEEM, M., SECKIN, S. & CLEMENS, N.T. 2017 Role of boundary-layer on unsteadiness on a Mach 2 swept-ramp shock/boundary-layer interaction using 50 kHz PIV. *55th AIAA Aerospace Sciences Meeting*. AIAA Paper 2017-0757.

WU, M. & MARTIN, M.P. 2008 Analysis of shock motion in shockwave and turbulent boundary layer interaction using direct numerical simulation data. *J. Fluid Mech.* **594**, 71–83.

WU, X. & MOIN, P. 2009 Direct numerical simulation of turbulence in a nominally zero-pressure-gradient flat-plate boundary layer. *J. Fluid Mech.* **630**, 5–41.

XU, S. & MARTIN, M.P. 2004 Assessment of inflow boundary conditions for compressible turbulent boundary layers. *Phys. Fluids* **16** (7), 2623–2639.

YU, M., CECI, A. & PIROZZOLI, S. 2022 Reynolds number effects and outer similarity of pressure fluctuations in turbulent pipe flow. *Intl J. Heat Fluid Flow* **96**, 108998.

ZUO, F.-Y., MEMMOLO, A., HUANG, G.-P. & PIROZZOLI, S. 2019 Direct numerical simulation of conical shock wave–turbulent boundary layer interaction. *J. Fluid Mech.* **877**, 167–195.

ZUO, F.-Y., MEMMOLO, A. & PIROZZOLI, S. 2021 Reynolds-averaged numerical simulations of conical shock-wave/boundary-layer interactions. *AIAA J.* **59** (5), 1645–1659.

ZUO, F.-Y. & MÖLDER, S. 2019 Hypersonic wavecatcher intakes and variable-geometry turbine based combined cycle engines. *Prog. Aerosp. Sci.* **106**, 108–144.

ZUO, F.Y., YU, M. & PIROZZOLI, S. 2022 Modal analysis of separation bubble unsteadiness in conical shock wave/turbulent boundary layer interaction. *AIAA J.* **60** (9), 5123–5135.